Melting behaviour of simulated radioactive waste as functions of different redox iron-bearing raw materials

RIGBY, Jessica, DIXON, Derek, CUTFORTH, Derek, MARCIAL, Jose, KLOUZEK, Jaroslav, POKORNY, Richard, KRUGER, Albert, SCRIMSHIRE, Alex <http://orcid.org/0000-0002-6828-3620>, BELL, Anthony <http://orcid.org/0000-0001-5038-5621> and BINGHAM, Paul <http://orcid.org/0000-0001-6017-0798>

This document is the Published Version [VoR]

Citation:

RIGBY, Jessica, DIXON, Derek, CUTFORTH, Derek, MARCIAL, Jose, KLOUZEK, Jaroslav, POKORNY, Richard, KRUGER, Albert, SCRIMSHIRE, Alex, BELL, Anthony and BINGHAM, Paul (2022). Melting behaviour of simulated radioactive waste as functions of different redox iron-bearing raw materials. Journal of Nuclear Materials, 569: 153946. [Article]

Journal of Nuclear Materials 569 (2022) 153946

Contents lists available at ScienceDirect

Journal of Nuclear Materials

journal homepage: www.elsevier.com/locate/jnucmat

Melting behaviour of simulated radioactive waste as functions of different redox iron-bearing raw materials

Jessica C. Rigby[a,*], Derek R. Dixon[b], Derek A. Cutforth[b], Jose Marcial[b], Jaroslav Kloužek[c,d], Richard Pokorný[c,d], Albert A. Kruger[e], Alex Scrimshire[a], Anthony M.T. Bell[a], Paul A. Bingham[a]

[a] Materials and Engineering Research Institute, College of Business, Technology and Engineering, Sheffield Hallam University, City Campus, Howard Street, Sheffield S1 1WB, UK
[b] Pacific Northwest National Laboratory, Richland, WA 99354, USA
[c] University of Chemistry and Technology Prague, Technicka 5, 166 28 Prague 6, Czech Republic
[d] Institute of Rock Structure and Mechanics of the Czech Academy of Sciences, V Holesovickach 41, 182 09 Prague 8, Czech Republic
[e] U.S. Department of Energy, Office of River Protection, Richland, WA 99352, USA

ARTICLE INFO

Article history:
Received 21 December 2021
Revised 18 July 2022
Accepted 24 July 2022
Available online 26 July 2022

ABSTRACT

Improved understanding of the mechanisms by which foaming occurs during vitrification of high-level radioactive waste feeds prior to operation of the Waste Treatment and Immobilization Plant at the Hanford Site, USA, will help to obviate operational issues and reduce the duration of the clean-up project by enhancing the feed-to-glass conversion. The HLW-NG-Fe2 high-iron simulated waste feed has been shown to exhibit excessive foaming, and the most recent predictive models overestimate the feed melting rate. The influence of delivering iron as a Fe^{2+}-bearing raw material ($FeC_2O_4{\cdot}2H_2O$), rather than a Fe^{3+} ($Fe(OH)_3$) material, was evaluated in terms of the effects on foaming during melting, to improve understanding of the mechanisms of foam production. A decrease of 50.0 ± 10.8% maximum generated foam volume is observed using $FeC_2O_4{\cdot}2H_2O$ as the iron source, compared with $Fe(OH)_3$. This is determined to be due to a large release of CO_2 before the foam onset temperature (the temperature above which the liquid phases forming are sufficiently viscous to trap the gases) and suppression of O_2 evolution during foam collapse. Structural analyses of simulated waste feeds after different stages of melting show that the remaining Fe^{2+} in the modified feed is oxidised to Fe^{3+} at temperatures between 600 and 800 °C. This feed was tested in a Laboratory Scale Melter with no excessive foaming or feeding issues. Analysis of the final glass products indicates that the glasses produced using the original HLW-NG-Fe2 feed using $Fe(OH)_3$ and the feed made with $FeC_2O_4{\cdot}2H_2O$ are structurally similar but not identical: the difference in the structure converges when the glass is melted for 24 h, suggesting a transient structure slightly different to that of the baseline in the glass produced using the reduced raw material.

1. Introduction

The Hanford site in Washington State, USA houses ~200,000 m^3 of radioactive legacy wastes in 177 carbon-steel tanks [1,2]. Now under construction and commissioning at the Hanford site is the Waste Treatment and Immobilization Plant (WTP), where High-Level Waste (HLW) and Low Activity Waste (LAW) streams from the tanks will be processed separately and vitrified in individual Joule Heated Ceramic Melters (JHCMs) [1,3–5]. Within these JHCMs the conversion of waste and process additives into molten glass will take place in a batch (raw material) layer (the "cold cap") on top of the melt pool [6,7]. While the cold cap can help to retain volatile species within the glass melt, foaming in the cold cap restricts heat transfer from the glass melt into the incoming feed slurry, thereby decreasing the feed melting rate [6,8–11]. Foaming occurs in the cold cap due to the evolution of gases from decomposition of the feed materials and redox reactions during feed-to-glass melt conversion. These gases then become trapped in the viscous melt and the reacting materials above the melt pool. Excessive foaming can both reduce the efficiency of the process and potentially lead to blockages of melter off-gas components [12]. Excessive foaming is therefore highly undesirable and thus control of foaming is a key process parameter.

---

* Corresponding author.
E-mail address: acespab@exchange.shu.ac.uk (J.C. Rigby).

https://doi.org/10.1016/j.jnucmat.2022.153946

Organic compounds have traditionally been added to radioactive waste feeds to mitigate excessive foaming and control redox state in industrial glass melting [6,13–19] and this approach has been successfully demonstrated in vitrification programs [20–24]. For high-nitrate Hanford Low-Activity Waste (LAW) feeds [24], which evolve both CO_x and NO_x during thermal decomposition, in the approximate temperature range 600–800 °C, sucrose has been accepted as the baseline reductant [14,25–27]. The evolution of CO_x and NO_x from these feeds during heating occurs as the feed materials begin to form a viscous melt, and is referred to as *primary foaming* [4,5,28,29]. Studies have shown the efficacy of sucrose in foam reduction in LAW feeds from both bench scale to research-scale melter tests, in reducing foam by denitration at 400 °C prior to melt connection and foam onset [29], and in retention of the volatile ^{99}Tc [27,30,31]. There has been a large output of work on sucrose addition to HLW feeds in other vitrification programs [17,32–35] but the applcation of reductants to Hanford HLW streams, generally higher in multivalent species than LAW feeds, is limited due to, potentially conservative, redox limits on the final glasses [14,36–38]. The management of organics in HLW feeds is important for controlling production rates and glass properties, however, the previous algorithms used to determine the amount of sugar to add to high-nitrate LAW feeds, based on the ratio of carbon to nitrogen in the feeds, need to be modified and required further testing [14].

Gases that evolve at high temperature, within the glass melt are usually the secondary fining gases O_2 and SO_2, with some residual CO_2 evolution. The trapping of the secondary fining gases beneath the highly viscous cold cap is *secondary foaming* [4,39,40]. Secondary foaming is much more prevalent in HLW streams with high contents of multivalent species such as Fe, Mn and Cr [4,39–40]. The distinction between primary and secondary foam can be difficult to observe for feeds high in multivalent species because of the continuous evolution of gas and overlapping reactions [41,42]. Due to the high-viscosity melt above the trapped gases, secondary foam does not readily collapse in the same way that primary foam does, and its removal can require additional measures such as vigorous bubbling [9,40,43].

From feed expansion tests, developed to analyse the amount of foaming in particular feeds during melting, it has been demonstrated that the high-iron HLW-NG-Fe2 simulated waste feed foams by up to 10 times its original volume during melting [44–46]. The HLW-NG-Fe2 glass composition, given in Table 1, was developed by the Vitreous State Laboratory (VSL) of the Catholic University of America to immobilise the Hanford high-iron C-106/AY-102 tank waste [47,48]. The final vitrified HLW-NG-Fe2 glass composition has 42 wt% waste loading and achieved an average glass production rate of 1650 kg m^{-2} day^{-1} in the DM100 research scale melter system at the VSL [45,47]. This melting rate is high compared to other feeds [45], however the most recent predictive models of melting rate using the Melt Rate Correlation equation, still overestimate the melting rate [49,50].

The Fe_2O_3 content, as well as the presence of Cr_2O_3 and NiO in the wastes, were limiting factors for waste loading due to spinel formation in the melter: spinel compounds such as magnetite, trevorite and chromite have commonly been found [47,51,52]. Iron-bearing spinel crystals are chemically durable and are therefore less of a concern for the quality of the final vitrified product, when present at levels of up to ~2 wt% [53]. However, these spinels can agglomerate and, due to their higher densities, settle to the bottom of the melter, which is intolerable in the JHCM melters as they are susceptible to clogging [54], as opposed to induction melters, such as those used in the UK, where a modest level of solid settling is considered acceptable [55]. The glass product discharged from the DM100 melter test contained only trace amounts of crystal precipitation upon melting and cooling, and 0.65 vol% spinel crystals containing Fe, Cr, Ni and Mn oxides were measured after heat treatment at 950 °C for 72 h [47] which is broadly consistent with being within the acceptable range of product quality (< 1 vol% of crystalline phases at 950 °C) [56,57].

Table 1
HLW-NG-Fe2 composition developed by the VSL to immobilise the C-106/AY-102 high-iron tank waste [43].

Raw Material	Batch/100 g	Oxide	Wt%
$Al(OH)_3$	8.61	Al_2O_3	5.59
H_3BO_3	0.56	B_2O_3	13.79
$Na_2B_4O_7{\cdot}10H_2O$	37.16	Na_2O	13.36
$CaCO_3$	0.94	CaO	0.52
CeO_2	0.12	CeO_2	0.12
$Cr_2O_3{\cdot}1{\cdot}5H_2O$	0.30	Cr_2O_3	0.25
$Fe(OH)_3$	20.54	Fe_2O_3	16.12
$La(OH)_3$	0.11	La_2O_3	0.09
Li_2CO_3	3.87	Li_2O	1.56
$Mg(OH)_2$	0.24	MgO	0.16
MnO_2	3.98	MnO_2	3.95
NaOH	0.81	NiO	0.47
Na_2CO_3	4.04	P_2O_5	0.78
$Ni(OH)_2$	0.59	PbO	0.63
$FePO_4{\cdot}2H_2O$	1.71	SO_3	0.22
PbO	0.63	SiO_2	41.02
Na_2SiO_3	8.03	SrO	0.20
Na_2SO_4	0.39	ZnO	0.03
SiO_2	37.33	ZrO_2	1.13
$SrCO_3$	0.28		
ZnO	0.03		
$Zr(OH)_4{\cdot}0{\cdot}654H_2O$	1.57		
$NaNO_2$	0.01		
$NaNO_3$	0.45		
$H_2C_2O_4{\cdot}2H_2O$	0.06		
Total	132.36	Total	100.00

Alternative iron-bearing waste simulant raw materials for the HLW-NG-Fe2 feed, to the standard $Fe(OH)_3$ slurry mixture (13 wt% $Fe(OH)_3$, 87% water), were explored by the VSL to study their effects on glass production rate and glass properties [58]. Alternatives included haematite (Fe_2O_3), magnetite (Fe_3O_4), goethite (FeO(OH)) and a mixture of all three. The mixture of iron sources provided the highest glass production rate of 1950 kg m^{-2} day^{-1}, followed by Fe_2O_3 at 1910 kg m^{-2} day^{-1}, Fe_3O_4 at 1830 kg m^{-2} day^{-1}, and finally FeO(OH) at 1725 kg m^{-2} day^{-1} [58]. The viscosity of the feed containing $Fe(OH)_3$ was an order of magnitude greater than the viscosities of any of the other feeds tested, it was concluded that the feed viscosity likely influenced the rate of melting [58]. Marcial et al. observed a correlation among these measured rates of melting and the fractions of chemically-bound water contributed by the iron sources, potentially leading to reduced melt viscosity and more rapid silica dissolution [59]. ^{57}Fe Mössbauer spectroscopy of the final vitrified glass products showed very little difference in the iron redox ratio, $Fe^{3+}/\Sigma Fe$, between glasses made with the different iron-bearing raw materials when melted in air at 1150 °C. The glass produced using Fe_3O_4 as a raw material presented $Fe^{3+}/\Sigma Fe = 0.994$ [58]. Since Fe_3O_4 contains 66.7% Fe^{3+} and 33.3% Fe^{2+}, these results suggested that most of the Fe^{2+} present in the feed material became oxidised during melting. No clear correlation was found between the redox states of iron in the starting raw materials and the glass production rate [58]. Crystallisation of spinels occurred in these glasses, forming between 0.1 and 0.5 vol%, and these spinel phases were mixtures of Fe, Cr, Mn and Ni oxides [58].

Previous studies applied ferrous oxalate as a raw material in an attempt to retain volatile species during vitrification of LAW feeds [27,60], which, as noted above, can exhibit different gas evolution profiles and foaming mechanisms to HLW feeds. Furthermore, these previous studies were generally performed in scaled melter systems with limited cold cap observation [27,60]. Exploration of the structural and morphological changes to feeds during melting, within the cold cap, and the properties that underpin the foam behaviour, have received more attention since 2011 with the development of the one-dimensional model of the cold cap [5] and more recent attempts to computationally model the dynamic cold cap system [40,61,62].

Two previous studies [44,63] investigated the use of an Fe^{2+}-bearing raw material, iron oxalate dihydrate ($FeC_2O_4 \cdot 2H_2O$), compared with Fe^{3+} iron hydroxide ($Fe(OH)_3$), in a simulated high-alumina waste feed (HLW-Al-19), with the aim of supressing foaming during vitrification. While it is not practical to change the iron raw material in this HLW-NG-Fe2 waste feed, as the iron originates in the waste, the results of these studies provide opportunity to explore and model the effects of redox state on the cold cap behaviour and better understand potential pathways for foam reduction. HLW-Al-19 is a HLW feed containing 24.02 wt% Al_2O_3, but only 5.91 wt% Fe_2O_3, which is significantly lower than the 16.01 wt% Fe_2O_3 present in the HLW-NG-Fe2 feed (Table 1) [44,63]. It also contains Bi_2O_3 and F, which are not present in the HLW-NG-Fe2 feed; and it does not contain CeO_2 or MnO which are present in the HLW-NG-Fe2 feed [63,47]. Consequently, direct comparisons between results for the two different feeds, whilst useful, must be made with caution. The HLW-Al-19 feed produced with iron oxalate dihydrate ($FeC_2O_4 \cdot 2H_2O$) as the iron source evolved no O_2 upon heating, compared with 1.2 g kg^{-1} of glass for the original feed prepared using iron hydroxide ($Fe(OH)_3$) as the iron source [44,63]. However, CO_2 release increased to 66.6 g kg^{-1} glass from the $FeC_2O_4 \cdot 2H_2O$ feed compared to 42.2 g kg^{-1} glass from the $Fe(OH)_3$ feed [63]. Following that study, X-ray absorption near edge spectroscopy (XANES) was employed to determine the oxidation states of the multivalent species present during melting of the different HLW-Al-19 feeds with $Fe(OH)_3$ and $FeC_2O_4 \cdot 2H_2O$ [44], whilst also exploring foaming behaviour and evolved gases. Again, the feed with $FeC_2O_4 \cdot 2H_2O$ showed no O_2 evolution above 900 °C by Evolved Gas Analysis (EGA), and the maximum foam volume decreased from ~4 to ~2.5 V(T) $V_G{}^{-1}$ (volume at temperature, T, divided by the final glass volume). However, the oxidation state of the iron in the raw material was found to have little effect on either the oxidation state or coordination of Fe at various stages of melting. The glass produced using the $FeC_2O_4 \cdot 2H_2O$ feed was only "slightly more reduced" than the original feed, with a statement that only a qualitative analysis was possible [44]. The same study also explored the oxidation states of Fe at different stages of melting of the HLW-NG-Fe2 feed [44]. During melting the amount of Fe^{2+} increased: the sample heated to 500 °C had $Fe^{3+}/\Sigma Fe = 1$. As the temperature increased this ratio decreased to a minimum of $Fe^{3+}/\Sigma Fe = 0.5$ in the glass sample and the average Fe coordination transformed from approximately five-fold to four-fold [44].

Based on the effects of the $FeC_2O_4 \cdot 2H_2O$ raw material on decreasing the foam volume in the HLW-Al-19 feed during heating [44,63], it is reasonable to anticipate that there may be an even greater effect on foam reduction when using $FeC_2O_4 \cdot 2H_2O$ as a raw material in the HLW-NG-Fe2 feed, with its substantially higher iron content. From this hypothesis the present study emerged, in which we aimed to investigate foaming of the HLW-NG-Fe2 feed during melting by the use of $FeC_2O_4 \cdot 2H_2O$ as raw material and thereby contribute towards developing a better understanding of mechanisms of foam reduction by investigating any changes in cold cap structure that may arise. Our study thus aims to support methods of redox control in the HLW streams, tailored to the mechanisms of foam generation, which can be anticipated to differ from those in LAW feeds, by investigating the highest iron Hanford waste feed, and how the redox state of the raw materials can influence the foam behaviour and structure during melting in these feeds.

Table 2
Iron-bearing raw material sources for HLW-NG-Fe2 and HLW-NG-Fe2-II feeds.

Feed	Raw Material	Batch/100 g	Oxide	wt%
HLW-NG-Fe2	$Fe(OH)_3$	20.54	Fe_2O_3	16.01
HLW-NG-Fe2-II	$FeC_2O_4 \cdot 2H_2O$	34.58	Fe_2O_3	16.01

2. Experimental procedures

2.1. Feed preparation

The HLW-NG-Fe2 feed, using NOAH Chemicals $Fe(OH)_3$ slurry mixture (99.9% purity, 13 wt% $Fe(OH)_3$, 87% water), as the iron source, was batched as shown in Table 1. The second feed, named HLW-NG-Fe2-II throughout, was batched with $FeC_2O_4 \cdot 2H_2O$ replacing the $Fe(OH)_3$ raw material on a wt% basis for the target Fe_2O_3 content, as described in Table 2. Both feeds were prepared at the Pacific Northwest National Laboratory (PNNL) on a 2 decimal place balance using > 99% purity raw materials. Chemicals were mixed with deionised water with a target glass yield was 400 g L^{-1} for HLW-NG-Fe2-II, and 290 g L^{-1} for HLW-NG-Fe2, the difference necessitated by the higher viscosity of the $Fe(OH)_3$-bearing slurry. Each feed was stirred continuously using a mechanical stirring rod during batching, and for 24 h afterwards to ensure homogeneity. ~1 L of feed was dried in an oven at 105 °C for 24 h and then milled in a steel vibration mill in preparation for analysis by further techniques; and the remainder of the slurry was stored for feeding into the Laboratory Scale Melter [64].

2.2. Stages of melting study samples

For each feed, 7 platinum crucibles containing 20 g of dried feed were heated in an electric furnace from room temperature to 600, 700, 800, 900, 1000, 1100 and 1150 °C at a rate of 10 °C min^{-1}. Once each temperature was attained, the crucible was removed from the furnace and quenched in air. Further glass samples were created by heating the dried feed to 1150 °C at a rate of 10 °C min^{-1} in platinum crucibles, dwelling for 1 h, then pouring the melt into steel ring moulds and annealing at 500 °C for 3 h, before cooling to room temperature at 2 °C min^{-1}.

2.3. Laboratory scale melter sample preparation

The Laboratory Scale Melter (LSM) at PNNL [64–66] was used to create a quenched cold cap representative sample of the HLW-NG-Fe2-II. The LSM demonstrates the formation of a cold cap inside a melter by partially submerging a fused silica melter vessel into a furnace on top of a platinum support for variable depth. A schematic is shown in Fig. 1, 200 g of the HLW-NG-Fe2-II glass was re-melted in the bottom of the melter vessel to form the melt pool. Continuously stirred slurry feed was then pumped into the top of the melter vessel at 8–10 mL min^{-1}, landing on top of the melt pool and creating a cold cap. Thermocouples recorded the temperature of the melt and plenum every 20 s during feeding to ensure that the melt temperature stayed at ~1150 °C, while the plenum temperature indicated cold cap coverage. After a sufficient cold cap was generated (~1 h of feeding), feeding was halted, and the entire melter vessel was removed from the furnace and quenched immediately in air by placing it on a copper block. Once cooled, the top of the vessel without any sample was removed, leaving a quenched cold cap sample encased in the silica vessel.

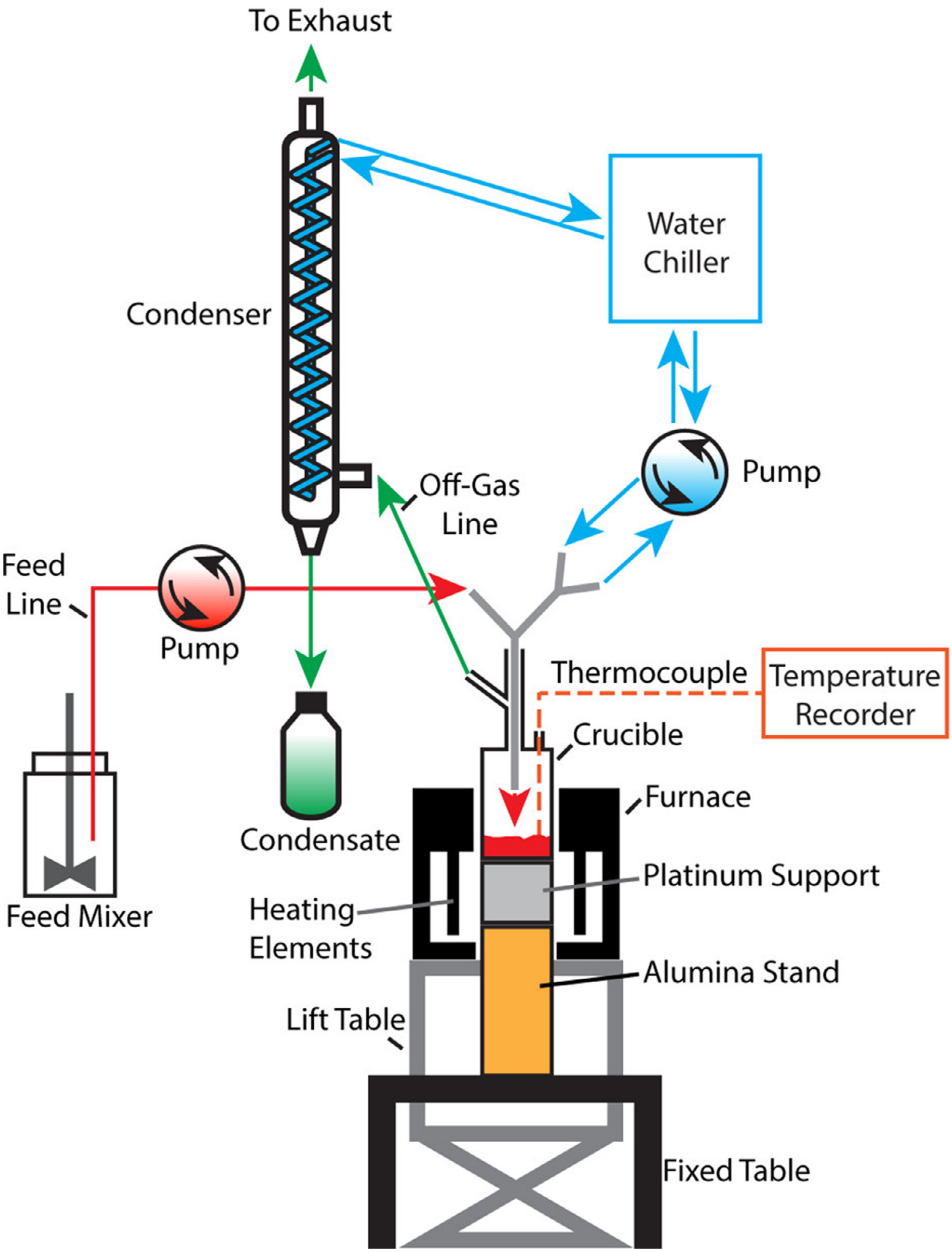

Fig. 1. Schematic of the laboratory-scale melter (LSM) [64].

2.4. Feed volume expansion testing

To quantify the amount of foaming of each feed during melting, pellets of dried feed, 13 mm in diameter pressed at 168 MPa, were heated at 10 °C min^{-1} from 25 to 1150 °C without dwelling in an electric furnace with an observation port. Photographs were taken at 100 °C intervals initially, and then at 10 °C intervals once the pellets began to change shape. Images were analysed via a MATLAB software program to calculate the normalised volume based on the assumption that the expansion was spherically symmetrical [68].

2.5. Thermal analysis

Thermogravimetric - Differential Thermal Analysis (TG-DTA) was performed on both the HLW-NG-Fe2 and HLW-NG-Fe2-II feed samples once dried powder had been generated, using a TA Instruments SDT Q600 Simultaneous Thermal Analyser. 30 mg of each dried feed sample was loaded into an alumina crucible and heated at 10 °C min^{-1} from room temperature to 1205 °C. The crucible mass was calibrated before the measurement with respect to a standard alumina crucible. Air was pumped through the furnace at a flow rate of 50 ml min^{-1}. Measurements of mass of the sample and the heat flow ($\mu W\ mg^{-1}$) were taken at 0.5 s intervals.

Thermogravimetric – Mass Spectrometry (TG-MS) using the Netzsch STA (Simultaneous Thermal Analysis) 409PG Luzz® coupled to an Aëleos mass spectrometer, observed the evolved gases during heating of the feeds. The furnace was heated at a rate of 10 °C min^{-1} from 30 to 1200 °C, with 40 ml min^{-1} of air pumped through the chamber, and the ion current was measured for each element of interest. For O_2 evolution the same process was carried out under a flow rate of 40 ml min^{-1} of N_2.

Evolved gas analysis (EGA) was performed on both the HLW-NG-Fe2 and HLW-NG-Fe2-II feeds at the Laboratory of Inorganic Materials, UCT Prague. ~1 g of each feed was heated at 10 °C min^{-1} from room temperature to 1160 °C in a silica gas tube within a furnace, under 50 ml min^{-1} He. The release rates of gases from the feeds were measured by Gas Chromatography – Mass Spectrometry, using an Agilent 6890 N/5973 N mass spectrometric detector.

2.6. Sample characterisation

2.6.1. Compositional analysis

For compositional analysis, the final glass samples were milled to a fine powder for X-ray fluorescence (XRF) spectroscopy. Approximately 1 g of each sample was mixed with approximately 10 g of $Li_2B_2O_7$ flux (doped with 0.5 wt% LiI anti-cracking agent). The mixture was loaded into a 90%Pt:10%Au crucible and melted at 1065 °C in a Claisse LeNeo fused bead maker furnace. The fused beads were analysed by XRF using a PANalytical MagiX PRO spectrometer with a Rh anode X-ray tube for elemental composition using an oxide analysis programme [68,69]. For B and Li elemental concentration, 500 mg of the samples were prepared by microwave digestion for ICP-MS on a Perkin Elmer ® Nexion-1000 ICP-MS.

2.6.2. X-ray diffraction

Samples for the Stages of Melting study were milled to a fine powder and loaded into flat plate X-ray powder diffraction (XRD) sample holders, which were then loaded onto a PANalytical X'Pert Pro X-ray powder diffractometer. Diffraction data were collected using Cu Kα X-rays with a power setting of 40 mA / 40 kV and samples were spun at 0.25 revolutions per second during data collection to improve the powder average. Diffraction patterns were collected over the angular range 5 to 80 º 2θ, with a step size of 0.0033 º 2θ and dwell time of 78.8 s per step. From the positions of the Bragg reflections in the diffraction patterns, crystalline phases were identified using the PANalytical HighScore Plus software [70] and the International Centre for Diffraction Data (ICDD) Powder Diffraction File database [71]. The relative abundance of each phase and the amorphous content was measured by intimately mixing 5 wt% Si with the ground sample and then performing XRD and comparing the relative abundances of other phases present using Rietveld refinement [72] in the HighScore Plus software.

2.6.3. Scanning electron microscopy/energy dispersive X-ray spectroscopy

Scanning electron microscopy and energy dispersive X-ray spectroscopy (SEM/EDX) were used to analyse the glass samples and to identify any crystalline precipitants and inhomogeneities. Samples were mounted in a conductive epoxy resin, ground with SiC abrasive paper to produce a flat surface, then polished using successive grades of 9, 6, 3 and 1 µm diamond paste. Polished samples were coated with a layer of carbon in a carbon coater for 600 ns, and conductive silver paint was applied to connect the sample to the metallic mount to ensure good electrical conduction and to avoid any charging on the sample surface during analysis. Samples were loaded into the FEI Quanta 650 FEG-ESEM operated at 20 kV and spot size, diameter of the final beam on the surface of the sample, of 3. Both secondary and backscattered electron images were taken of each sample at different magnifications. On areas of interest images were processed using Aztec EDX software, where point scans for elemental compositions and elemental maps were taken.

2.6.4. Raman spectroscopy

For analysis of structural changes during melting, polished samples from the Stages of melting study were analysed using a Renishaw InVia Raman Spectrometer fitted with a CCD detector and a 532 nm laser at 10 mW power and x10 objective lens. Raman spectra were collected at Raman shifts between 100 and 3000 cm^{-1} with 15 accumulations and an exposure time of 20 s for each accumulation. All spectra underwent a baseline correction, a 5th order polynomial fluorescence correction, and a temperature and frequency dependent scattering intensity correction [73].

2.6.5. ^{57}Fe Mössbauer spectroscopy

For analysis of the local environment and oxidation state/s of iron during melting, the samples heated to 800, 1000 and 1150 °C for each of the feeds were powdered for room temperature ^{57}Fe Mössbauer spectroscopy. The 14.4 keV γ-rays from the decay of a 25 mCi ^{57} Co source in Rh matrix oscillated at constant acceleration were absorbed by the sample. ^{57}Fe Mössbauer spectra were collected in the velocity range of ±12 mm s^{-1} relative to α-Fe. The signal-to-noise ratio was improved with data collection times of up to two weeks. The Recoil software package [74] was used to fit the data with either Lorentzian fits or xVBF, and the assumption was made that the recoil-free fraction ratio $f(Fe^{3+}/Fe^{2+}) = 1.0$ when estimating redox ratios from fitted spectral areas.

3. Results

3.1. Feed expansion tests and gas evolution

From the feed expansion test results shown in Fig. 2, there is a 49.8% reduction in maximum volume expansion using $FeC_2O_4{\cdot}2H_2O$, equating to a reduction in maximum porosity of 11.0%. A peak volume expansion of ~10 times the volume of glass in the HLW-NG-Fe2 feed is in close agreement with the previous studies [44–46]. The total gas evolved in each feed, obtained from the derivative of the mass loss from TGA, shows a 62.9 ± 2.8% increase during melting in the HLW-NG-Fe2-II feed compared with the original.

The H_2O and CO_2 evolution are both greater in the HLW-NG-Fe2-II feed, Fig. 3, than from the HLW-NG-Fe2 feed. Dehydration of raw materials in both feeds aligns with an exothermic peak at ~280 °C in the DTA curves. The CO_2 evolution from the HLW-NG-Fe2-II feed also corresponds to endothermic reactions shown in the DTA curve between ~400 and 550 °C which are not present in the DTA curve for the original feed. The increase in CO and CO_2 evolution in the HLW-NG-Fe2-II feed compared with the original is expected due to the added C in the raw material. O_2 is evolved from the original feed in spikes at 736, 772 and 807 °C, which corresponds to sharp exothermic peaks in the DTA curve. Strong peaks have been observed during O_2 consumption reactions of transition metals, such as the exothermic reaction $MnO_2 \rightarrow Mn_2O_3$ [75]. These peaks and the associated O_2 peaks are not present in the data for the original HLW-NG-Fe2-II feed. The SO_2 evolution is also suppressed in the modified ($FeC_2O_4{\cdot}2H_2O$) feed.

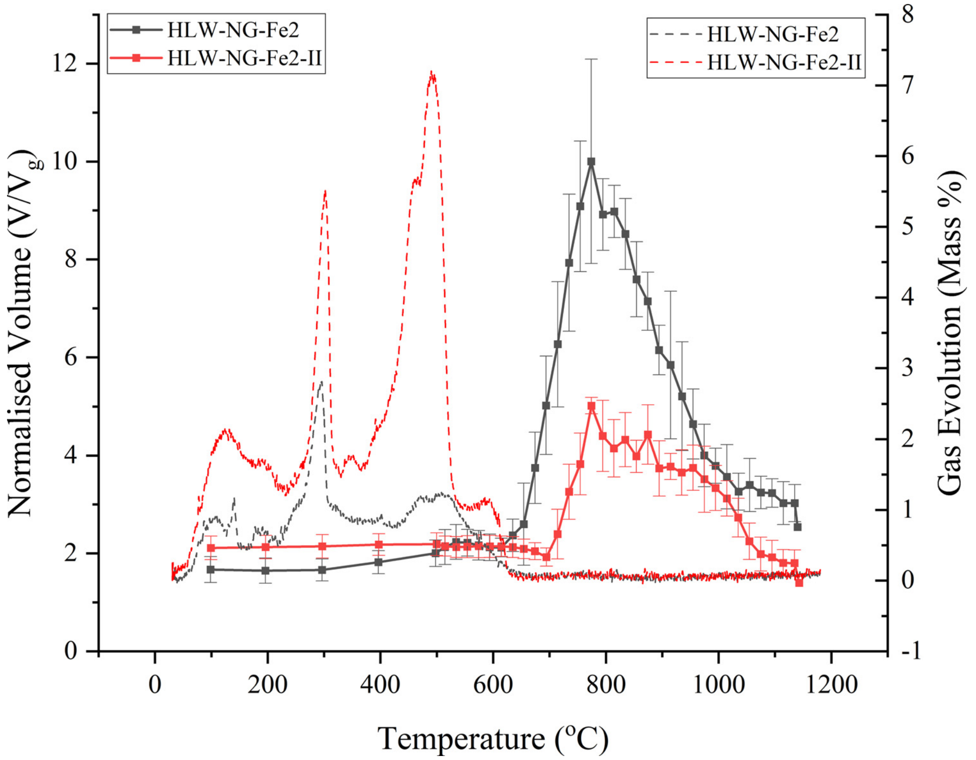

Fig. 2. Volume expansion curves normalised to the volume of glass, V/V_g, (solid lines) during melting of a pellet of the HLW-NG-Fe2 (black) and HLW-NG-Fe2-II (red). Total gas evolution (dashed lines) obtained by differentiating mass losses from TGA (For interpretation of the references to color in this figure, the reader is referred to the web version of this article.).

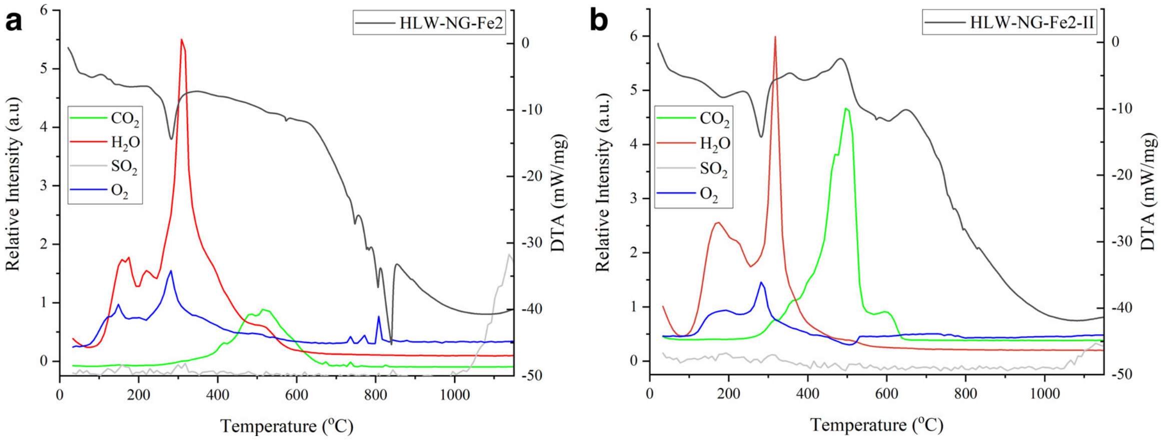

Fig. 3. Evolved gases by Thermogravimetric Mass Spectrometry (left axis) of H_2O, CO_2, O_2 and SO_2 and Differential Thermal analysis (right axis) for the HLW-NG-Fe2 and HLW-NG-Fe2-II feeds. SO_2 is scaled x 500.

Assuming an equal evolution of gases from other raw materials, the oxidation of FeO to Fe_2O_3 by 1150 °C, and no further oxygen consumption/evolution, an increase of 42.29 g kg^{-1} CO_2, and 80.75 g kg^{-1} glass CO, is expected stoichiometrically from the $FeC_2O_4 \cdot 2H_2O$ raw material during melting compared to the $Fe(OH)_3$ source. The CO_2 evolution shows an increase of 141.10 g kg^{-1} glass, and the CO evolution an increase of only 35.17 g kg^{-1} glass, leading to the assumption that oxygen is consumed during the decomposition reactions from elsewhere in the melt, forming more CO_2. Peak evolution of both CO and CO_2 occurs before the foam onset temperature of 600 °C in the HLW-NG-Fe2-II feed. The suppression of O_2 evolution in the HLW-NG-Fe2-II feed compared to the 5.12 g kg^{-1} of glass evolved during melting of the HLW-NG-Fe2 feed is clearly defined in Fig. 4, the lack of O_2 evolution is expected as the added carbon forming CO and CO_2, and the change from FeO to Fe_2O_3, provide a negative overall oxygen balance [20,76].

3.2. X-ray diffraction

The phase assemblage of the samples produced during the Stages of Melting study, between foam onset and melting temperatures (600–1150 °C), were analysed by XRD with Rietveld refinement for identification of the phases present and estimation of the relative abundances of the crystalline phase and the amorphous phase content. Fig. 5 shows the X-ray powder diffraction patterns for the Stages of Melting samples of each feed, quenched between 600 and 1150 °C, and Fig. 6 shows the phases identified and quantified by Rietveld refinement for each of these samples, as well as the amorphous phase fraction.

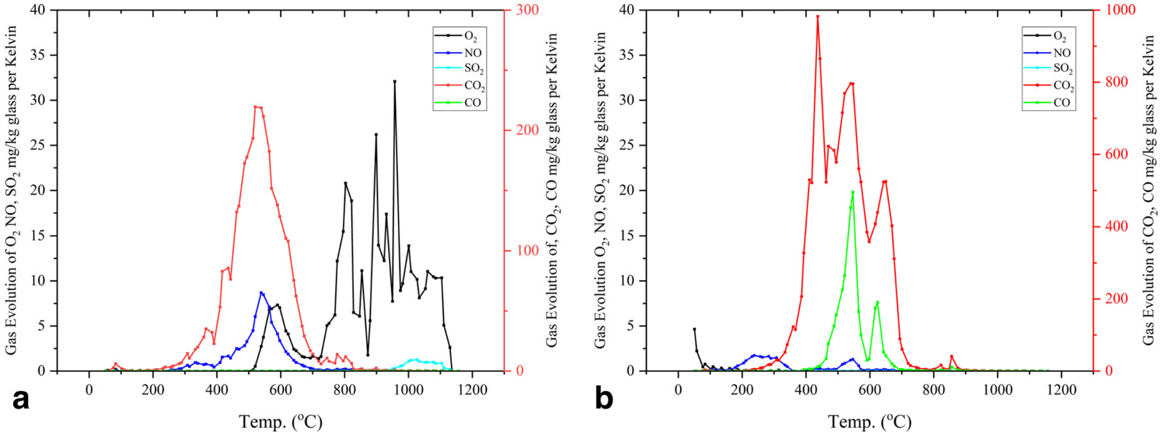

Fig. 4. Evolved Gas Analysis (EGA) of NO, H_2O, CO_2, O_2 and SO_2 for the HLW-NG-Fe2 (left) and HLW-NG-Fe2-II (right) feeds.

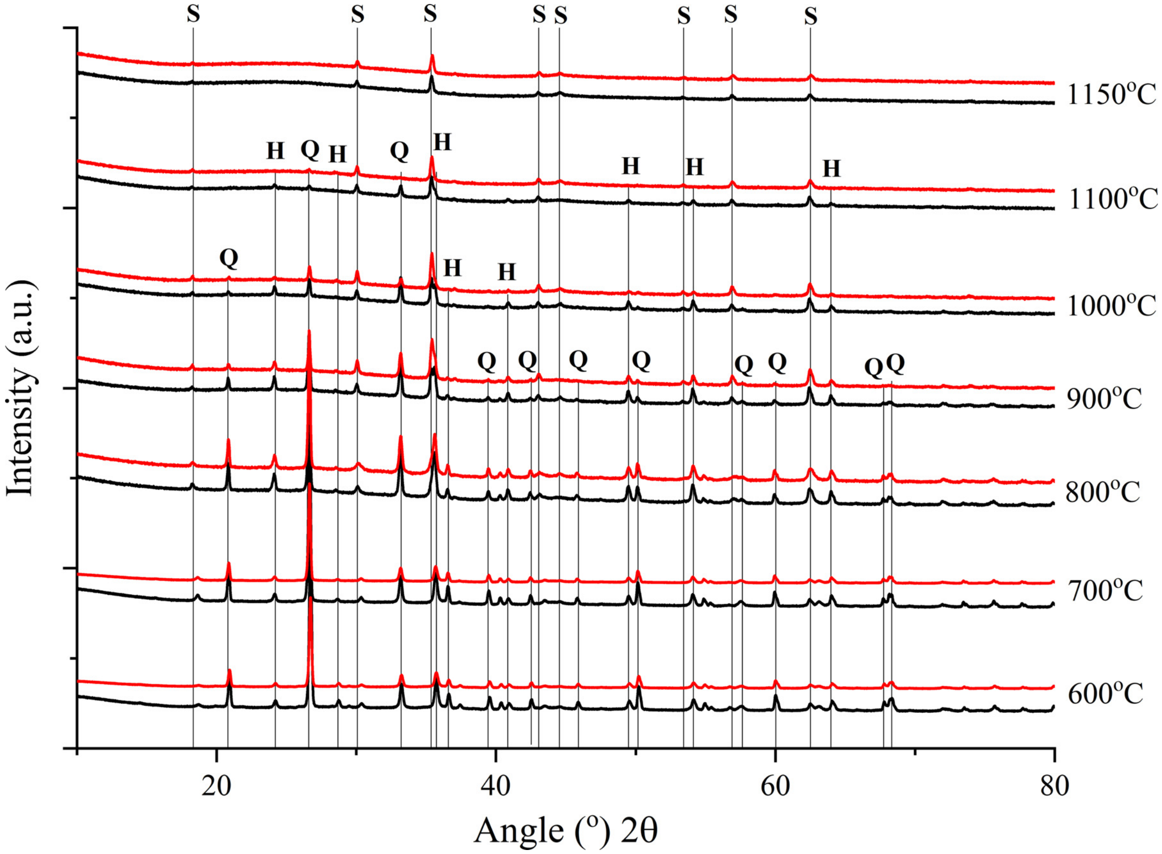

Fig. 5. Comparison of XRD patterns for HLW-NG-Fe2 (black) and HLW-NG-Fe2-II (red) stages of melting samples quenched at 600, 700, 800, 900, 1000, 1100 and 1150 °C. Peaks identified as belonging to Haematite ICDD; 04-015-7029, Quartz ICDD; 01-070-3755, and Magnetite ICDD; 04-009-8433, phases are labelled H, Q and S, respectively (For interpretation of the references to color in this figure, the reader is referred to the web version of this article.).

Quartz dissolution is similar in both feeds and compares with the previous measurements of quartz [59]. At 1150 °C the quartz has completely dissolved in both feeds. Haematite, present from 600 to 1100 °C in the HLW-NG-Fe2 feed, indicates that the decomposition of the $Fe(OH)_3$ raw material has been completed below 600 °C. After reaching a maximum relative abundance at 800 °C, haematite dissolves into the melt and has fully dissolved by 1150 °C. Both haematite and magnetite have been found as crystalline phases present in the vitrified samples produced from HLW-NG-Fe2 feed during previous melter runs [58]. In the HLW-NG-Fe2-II samples there are no crystalline Fe-containing phases present at 600 °C. At 700 °C there is a significant amount of spinel phase formed which decreases at 800 °C when haematite forms. Less haematite and more magnetite are present in the HLW-NG-Fe2-II samples from 800 to 1150 °C.

Rietveld refined lattice parameters of the spinel-type structures identified are given in Tables 5 and 6. All of the structures are $Fd\bar{3}m$ cubic spinel structures [77], in the magnetite series, with Fe usually occupying the B-site in the typical structure AB_2O_4 [77,78]. At 1150 °C both glasses contained phases identified as Magnetite (Fe_3O_4) with lattice constants ($a = b = c$) of 8.401(4) Å for the HLW-NG-Fe2 glass and 8.391(2) Å for the HLW-NG-Fe2-II glass. These are close to the referenced lattice constants for Fe_3O_4 at 8.394 Å [78]. The differences in the lattice parameters suggests

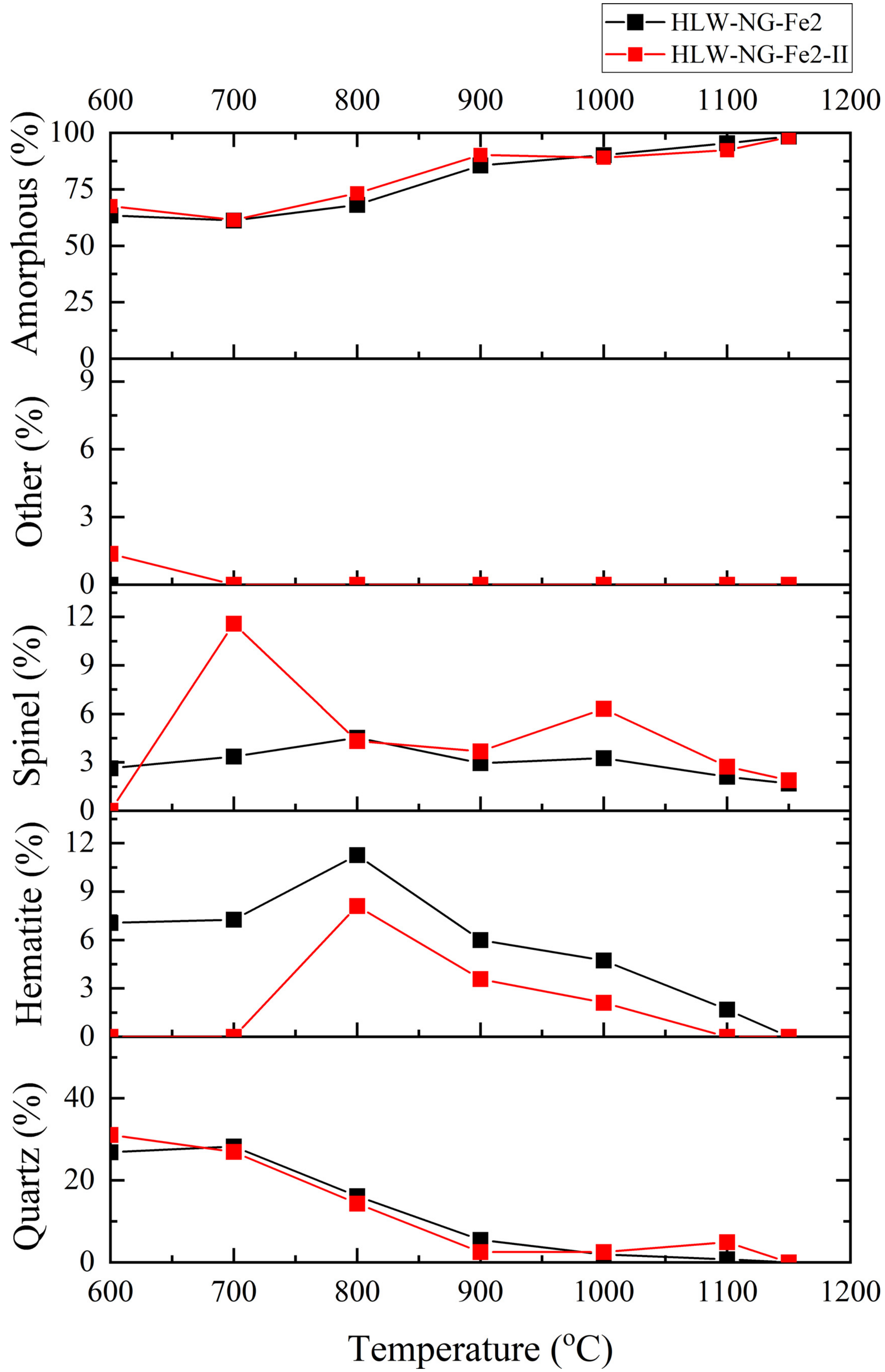

Fig. 6. Comparison of quantity of phases present during melting by Rietveld refinement of X-ray powder diffraction patterns in HLW-NG-Fe2 (black) and HLW-NG-Fe2-II (red). Quartz ICDD: 01-070-3755, Haematite ICDD: 04-015-7029, "Other" phase in the HLW-NG-Fe2-II feed identified as Baddeleyite (ZrO_2), ICDD: 04-007-2132. "Spinel" incorporates cubic spinels based on the magnetite system, Fe_3O_4. Error bars are contained within the data points (For interpretation of the references to color in this figure, the reader is referred to the web version of this article.).

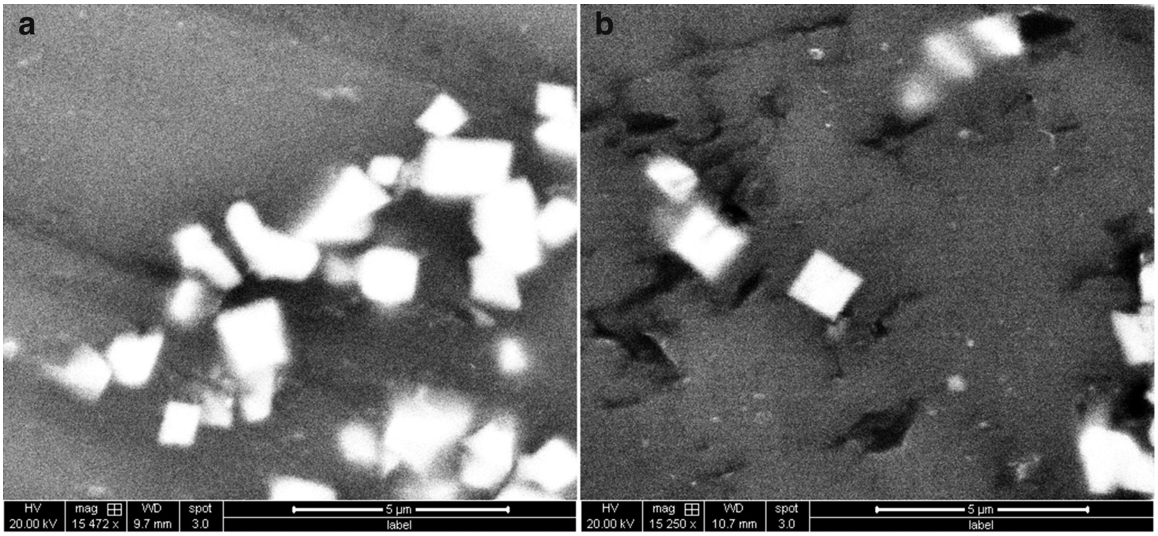

Fig. 7. Secondary electron images of the spinel crystals present in the samples heated to 1150 °C in (a) the HLW-NG-Fe2 feed and (b) HLW-NG-Fe2-II feed.

other elements such as Cr, Ni or Mn may be present as solid solutions with Fe in these compounds. This is investigated in the next section by SEM/EDX.

3.3. SEM/EDX

Further investigation of the of the spinel phases identified by XRD, using SEM/EDX on the samples heated to 1150 °C, shows an example of the cubic shape of these crystals in the HLW-NG-Fe2 and HLW-NG-Fe2-II samples, given in Fig. 7. The crystals are of similar size in both samples, with an average extrapolated volume of 1.39 μm^3 and 1.31 μm^3 for the HLW-NG-Fe2-II and HLW-NG-Fe2 samples, respectively, calculated from the images using image analysis software (ImageJ) [79].

Elemental mapping by energy dispersive spectroscopy (EDX) of these spinel phases and the surrounding glass matrix, shown in Figs. 8 and 9, confirms that Cr, Mn, Ni and Fe are all present at substantially elevated levels in the cubic crystals compared with the surrounding glass. Full results of EDX point scans to determine semi-quantitative compositions of the crystals in the HLW-NG-Fe2 glass are given in Appendix A. The average composition of the cubic crystals was 37.3 at% Fe, 32.1 at% O, 9.5 at% Ni, 6.1 at% Cr, 6.3 at% Mn, 4.5 at% Si, 2.6 at% Na, 1.0 at% Al. Due to the interaction volume of the dispersed X-rays it is likely that this also incorporates some of the amorphous region, explaining the low values for Si and Na. The crystals in both glasses contain the same elements and, from the average composition, these crystals contain mostly Fe and O. The smaller contents of Ni, Cr and Mn are consistent with the aforementioned hypothesis that these elements are situated on some of the sites within a mostly magnetite cubic spinel structure.

3.4. Raman spectroscopy

The Raman spectra, Fig. 10, allow insight to the structure of the glassy phase and how the iron is bonded within the network, together with information on some crystalline phases present. Whilst full deconvolution of the spectra would be very difficult, given the number of components and the presence of both amorphous and crystalline phases, general indicators of bonding within the borosilicate glass network can be obtained from the profile of the Raman spectra for feeds heated to 1000 °C and above.

Consistent with the X-ray powder diffraction data, which shows the development of the amorphous phase with increasing temperature (Figs. 5 and 6), the wide Raman Si-O (Al-O, Fe-O) Q-species region, between ~800 and 1200 cm^{-1} [80,81], emerges as the temperature increases, as well as bands due to the (boro)silicate network and borate rings between 350 and 600 cm^{-1} and the boron species bands at ~1200 to 1500 cm^{-1} expected for borosilicate glasses [80,81]. The major glass melt formation, the emergence of these bands and broadening of narrow crystalline bands, appears to occur earlier in the HLW-NG-Fe2 feed, between 800 and 900 °C; and occurs slightly later, between 900 and 1000 °C, in the reduced feed. Rietveld refinement of the X-ray powder diffraction patterns for the samples obtained in this temperature range provide no evidence that could indicate a difference in melting rate of the two feeds, the dissolution of silica and the amorphous phase fraction is similar throughout. However, these Raman data might suggest retardation in the structural formation of the glass melt with the use of $FeC_2O_4{\cdot}2H_2O$ as a raw material. Narrow Raman bands, indicative of crystalline phases, are generally broadened or absent from the spectra for samples heated above 1000 °C. The narrow Raman band ~1550 cm^{-1} present in all spectra is consistent with the stretching mode of the O–O bond in molecular oxygen [82].

Between 900 and 1150 °C the most significant difference between the two feeds is the narrow Raman band at 610 cm^{-1}. The Raman difference spectra for the 1150 °C HLW-NG-Fe2-II glass compared with the 1150 °C HLW-NG-Fe2 glass shown in Fig. 11. displays the large difference between the two samples in this spectral region, and also more minor shifts in the convoluted bands in the ~800–1200 cm^{-1} (Si-O Q^n) region and some changes at higher Raman shifts of ~1200–1500 cm^{-1}.

The Raman spectrum of crystalline magnetite exhibits its main, narrow band at ~670 cm^{-1} [83,84], with other bands being much less intense. Given the content of spinel crystals in the glass samples obtained from Rietveld analysis, a small Raman band in this region would not be surprising, and perhaps a small change in the centroid Raman shift of this band could be described by a difference in the crystal lattice compared to pure magnetite through the solid solution of Ni, Cr or Mn atoms in the spinel structure. However, the spinel contents are not significantly different between the two samples, yet the intensity of the Raman band at 610 cm^{-1} is substantially different, suggesting other origins.

A similar change in intensity of a Raman band at ~610 cm^{-1} was observed in sodium borosilicate glasses containing iron [85] and a decrease in intensity was observed with both an increase in iron content and with an increase in $Fe^{3+}/\Sigma Fe$, how-

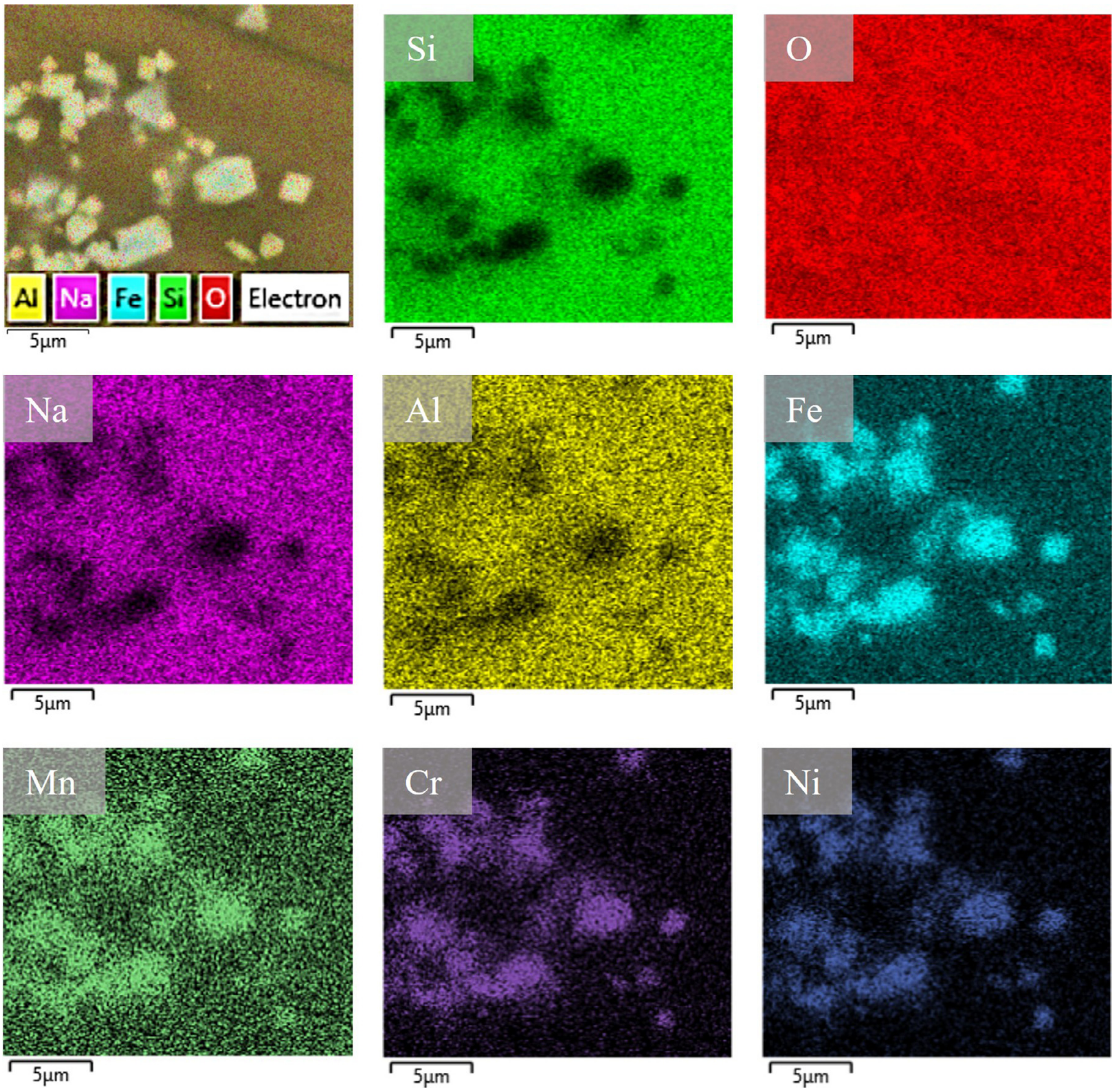

Fig. 8. Elemental maps by Energy Dispersive X-ray Spectroscopy of the HLW-NG-Fe2 sample heat-treated to 1150 °C.

ever, that particular Raman band was not discussed in that study. Further studies have attributed this band to danburite ring structures [86,87], which are shown to change in shape and intensity with iron content and iron oxidation state [85], based on a similar mechanism to the Yun and Bray model for the effects of Al_2O_3 concentration in sodium borosilicate glasses [86,88], and the Na^+ cations will preferentially charge-compensate Fe^{3+} in tetrahedral coordination [88,89]. The high-frequency Raman envelope, 1200–1400 cm^{-1}, due to $BO_2O^{-}BO_3$ units, also shifted to a lower Raman shift with an increase in Fe^{2+} content [88], which is not observed in the Raman spectra for the samples studied here, shown in Fig. 11. Furthermore, no significant structural differences have been observed in the two samples by X-ray powder diffraction.

To investigate further, the HLW-NG-Fe2-II sample was remelted at 1150 °C for 24 h to determine whether the behaviour of the ~610 cm^{-1} Raman band was transient or remained after longer melting times. Fig. 12 shows a comparison between the Raman spectra of the original HLW-NG-Fe2-II glass melted at 1150 °C for one hour, and the remelted glass at 1150 °C for 24 h. Some decrease in the intensity of the 610 cm^{-1} peak is observed, but not to the level of the other sample. This may suggest that some form of structural relaxation or equilibration may be taking place and the glass may be slowly approaching an equilibrium state in terms of redox, partitioning of iron or its complexation with other species as discussed above, or other structural motifs beyond the scope of the present study. Within the typical melter residence time of the JHCM, nominally 65 h [90,91], such equilibrations may occur [92], but further research is required to elucidate the behaviour of this Raman band and its intriguing, and apparently transient, structural origin.

3.5. Mössbauer spectroscopy

^{57}Fe Mössbauer spectra were collected for the samples quenched at 600, 800, 1000 and 1150 °C. The fitted spectra are shown in Fig. 13. Hyperfine fitting parameters for the samples are presented in Table 7. For the original HLW-NG-Fe2 feed the iron in the sample heated to 600 °C is mostly present in crystalline magnetic phases, with sextets corresponding to α-Fe_2O_3 [93] and spinel structures [94,95], consistent with the results of XRD. The content of paramagnetic phase, with a relative spectral area of 9%, in the HLW-NG-Fe2 feed at 600 °C, has centre shift (CS) and quadrupole splitting (QS) values of 0.33 and 1.12, consistent with octahedrally coordinated Fe^{3+} [94,95] which may reside within the

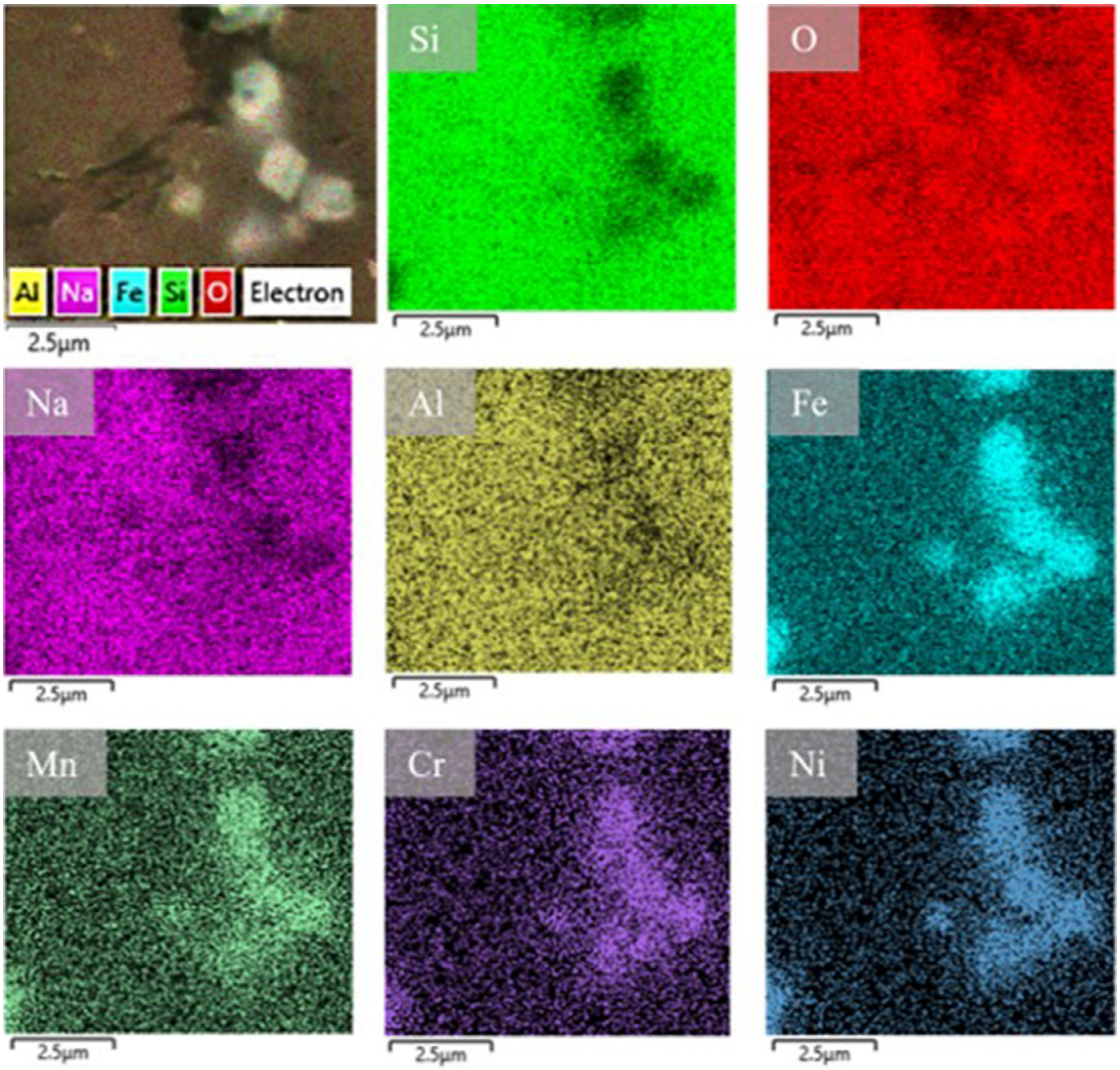

Fig. 9. Elemental maps by Energy Dispersive X-ray Spectroscopy of the HLW-NG-Fe2-II sample heat-treated to 1150 °C.

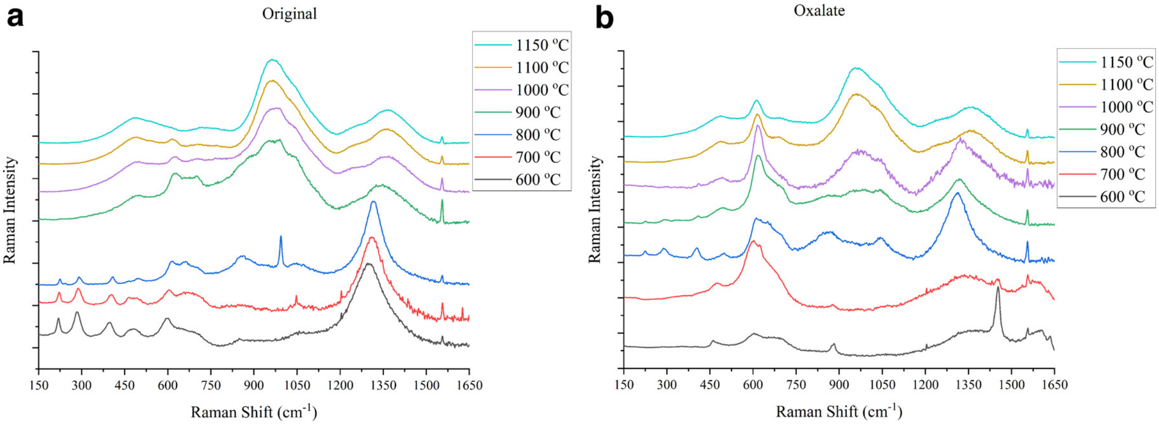

Fig. 10. Raman spectra of the (a) HLW-NG-Fe2 and (b) HLW-NG-Fe2-II feeds during melting at 600, 700, 800, 900, 1000, 1100 and 1150 °C.

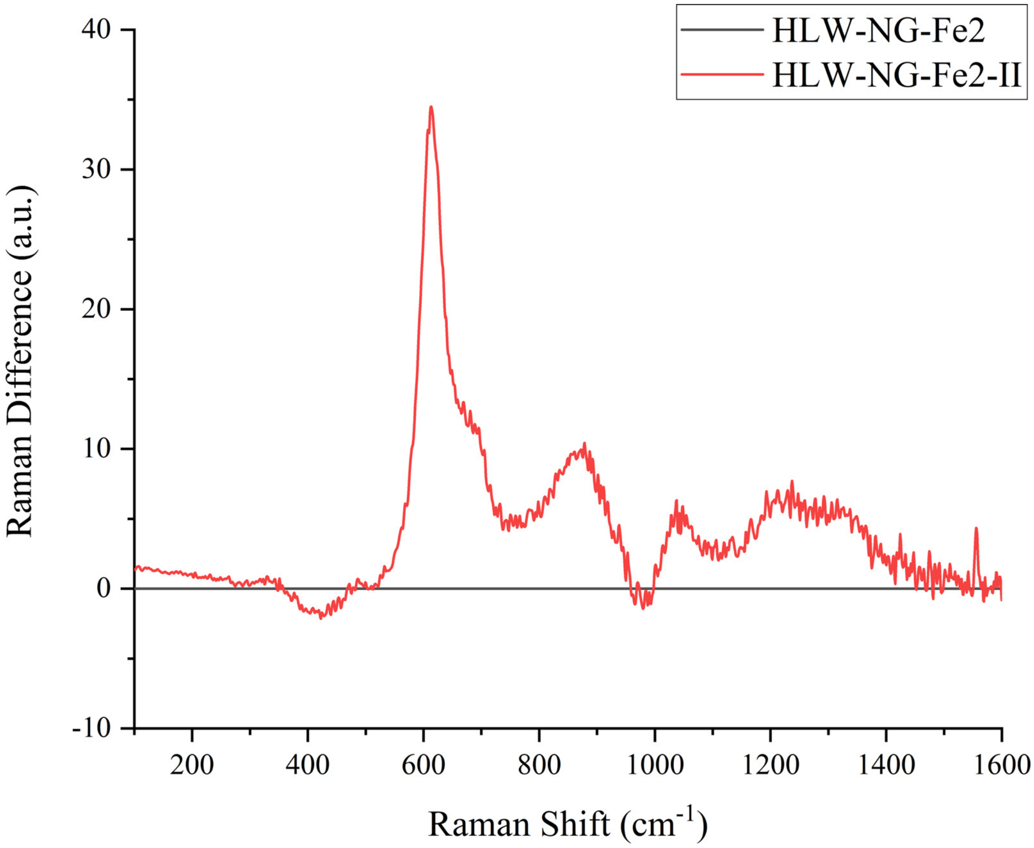

Fig. 11. Raman Difference spectrum for HLW-NG-Fe2-II relative to HLW-NG-Fe2 ($y = 0$).

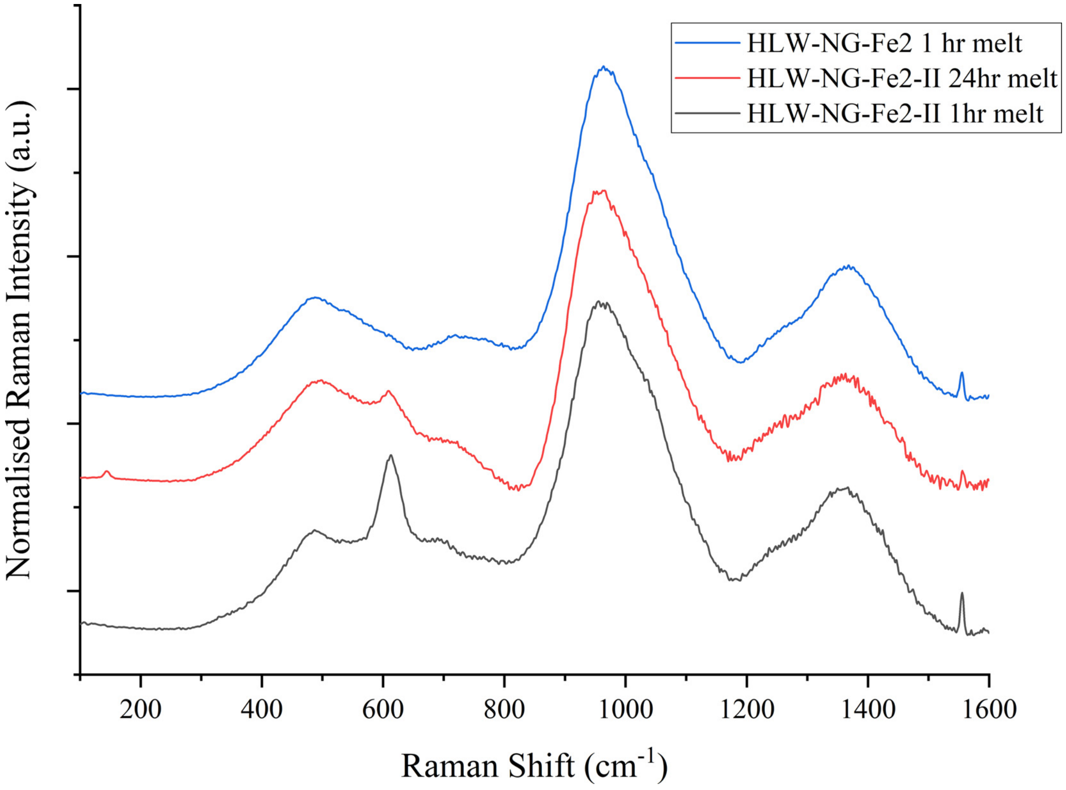

Fig. 12. Raman spectra of the HLW-NG-Fe2 glass, and the HLW-NG-Fe2-II glasses melted for 1 and 24 h.

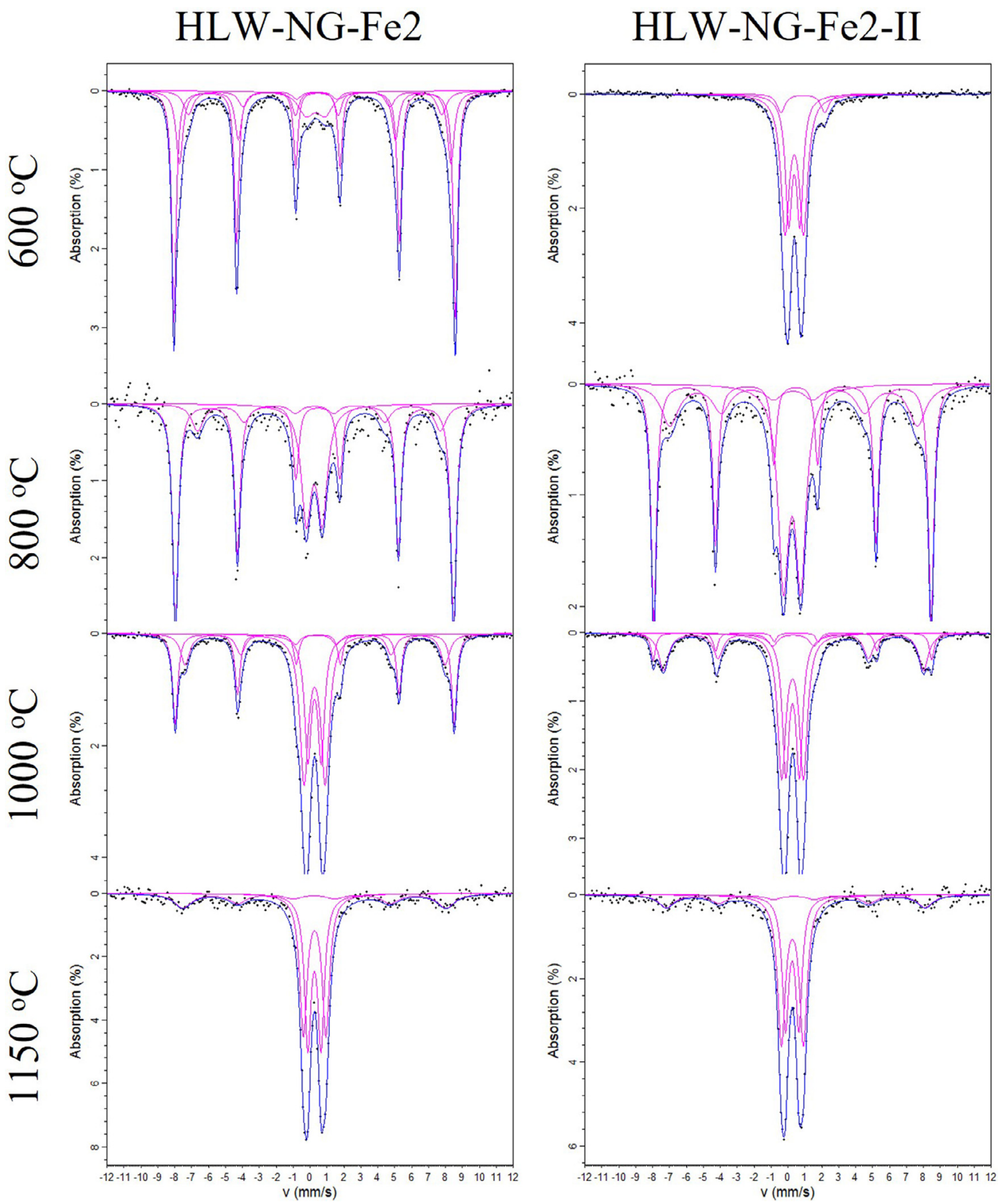

Fig. 13. Room temperature ^{57}Fe Mössbauer spectra for heat-treated feed samples at 600, 800, 1000 and 1150 °C fitted with Lorentzian functions for the HLW-NG-Fe2 and HLW-NG-Fe2-II feeds. CS relative to α-Fe.

amorphous phase shown to be present (Figs. 5 and 6). As the temperature increases, the relative abundance of paramagnetic phase increases (consistent with increasing amorphous content, Fig. 6) and a second doublet emerges with CS and QS parameters of 0.27 and 0.79, respectively, consistent with tetrahedral Fe^{3+} [94–96], while the sextets arising from the crystalline phases decrease in intensity, leaving only a small sextet at 1150 °C.

For the reduced feed HLW-NG-Fe2-II, the iron in the sample can be fitted by 3 paramagnetic doublets. Two of these doublets are consistent with octahedral Fe^{3+} in the amorphous phase, while the third is associated with tetrahedral Fe^{2+}, in FeC_2O_4 - at room temperature a doublet is expected with an CS $\sim$ 1.12 mm s^{-1} and QS $\sim$ 1.72 mm s^{-1} [97,98]. The Fe^{2+} doublet presented here has CS $\sim$ 0.89 and QS $\sim$ 2.59 mm s^{-1}, suggesting that the Fe^{2+} ions are tetrahedrally coordinated, rather than the octahedrally coordinated iron in FeC_2O_4 at room temperature. The distortion in the geometry affecting QS; and the CS is more representative of unstable FeO [99,100]. At 800 °C crystalline haematite and spinel phases are present (Figs. 5 and 6). Haematite has a higher relative abundance at 800 °C than it does in the 800 °C HLW-NG-Fe2 spectra, however, at 1000 °C the haematite in the HLW-NG-Fe2-II sample has decreased more significantly, reflecting the relative abundances of the phases determined by XRD (Figs. 5 and 6). The paramagnetic Fe^{3+} phases in both samples generally change their hyperfine parameters to illustrate more tetrahedrally coordinated Fe^{3+} with increasing temperature [96,101].

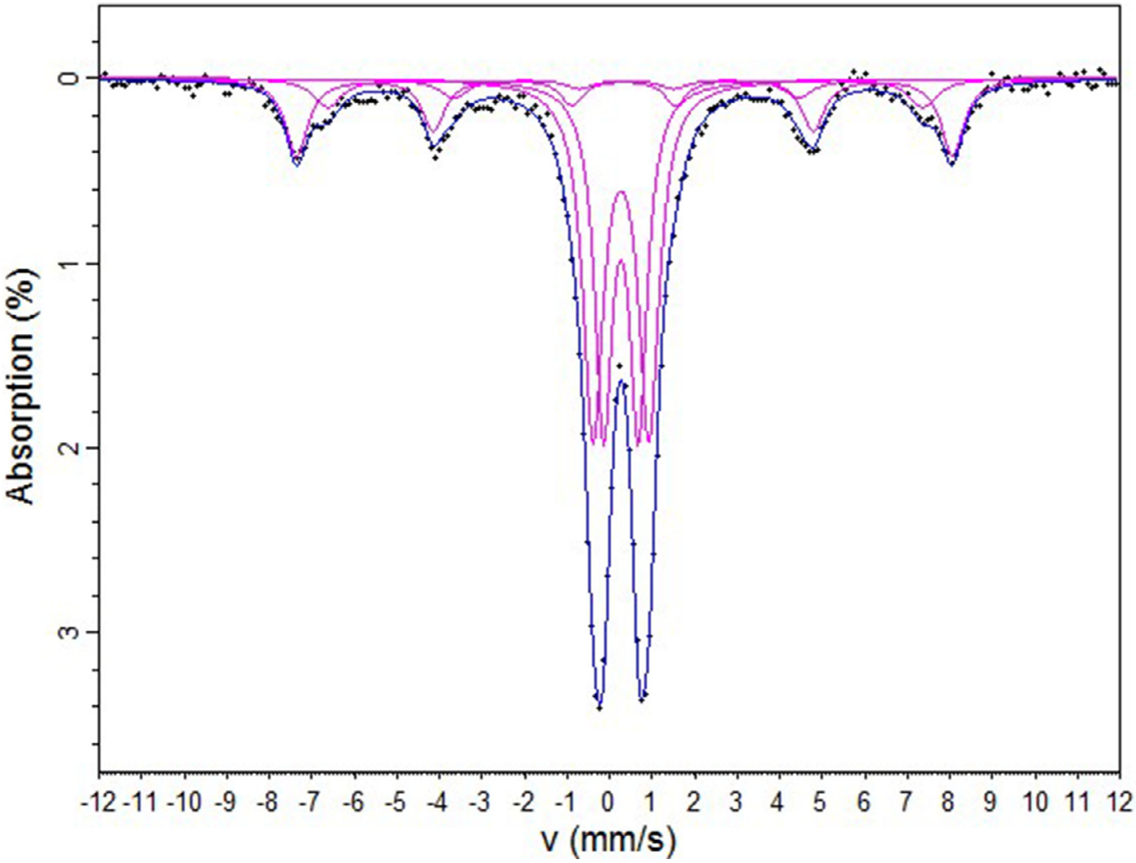

Fig. 14. Room temperature ^{57}Fe Mössbauer spectrum for HLW-NG-Fe2-II glass sample heated to 1150 °C for 24 h fitted with Lorentzian functions. CS relative to α-Fe.

At 1150 °C the paramagnetic phases in each sample are consistent with tetrahedrally coordinated Fe^{3+} in the bulk amorphous glass [96,101], the paramagnetic phases with the higher QS, ~1.3, has a higher relative abundance in the HLW-NG-Fe2-II sample than the original where the two doublets are almost equal in area. The remaining sextets fitted to spectra for both samples are almost identical. Both have CS and QS that are similar to values for the two sites of Fe_3O_4, which has an A-site at CS = 0.32 mm s^{-1} and H = 49.5 T, and a B site at CS = 0.66 mm s^{-1} and H = 45.6 T [93,95,102,103]. Chromite ($FeCr_2O_4$), wherein Fe^{2+} occupies the A site and Cr^{3+} the B site, presents itself as a Mössbauer singlet with a high CS ~0.937 mm s^{-1} in room temperature Mössbauer spectra [104], the presence of Cr^{3+} ions generally reduces the strength of the A-O-B magnetic interactions, instead coupling anti-ferromagnetically with the Fe ions [105,106]. Those spinels with Fe^{3+} occupying the B site, such as $Ni_{0.6}Zn_{0.4}FeO_4$, produce sextets with CS ~ 0.25 and 0.36 mm s^{-1} and H = 49.1 and 52.4 T [107]. Similarly, for $MnFe_2O_4$, with negligible Fe^{2+} ions in the A site, CS ~ 0.51–0.57 mm s^{-1} and H ~ 410–460 kOe [108] have been observed. In the spectra shown in Fig. 13, the sextet indicates that at least some Fe^{3+} occupies the B site in the spinel. As shown by the EDX in Fig. 9 there are also other multivalent species contained in the spinel structure, explaining the slight mismatch with magnetite. The relative amounts of spinel to paramagnetic phase, is extremely low (Figs. 5 and 6), which limits the resolution of the spinel sextet in the Mössbauer spectra.

Fig. 14 displays the spectra, and Table 8, the hyperfine fit parameters for the HLW-NG-Fe2-II sample after 24 h of melting. There appears to be a difference in the relative abundance of the paramagnetic doublets, there is an increase in the proportion of the doublet with the higher QS ~1.3 mm s^{-1}, suggesting some equilibration towards the HLW-NG-Fe2 sample. However, further xVBF fits of the HLW-NG-Fe2-II and HLW-NG-Fe2 24 h melt samples demonstrated no significant difference in partitioning of the iron in the total paramagnetic phase, with CS = 0.26 and QS = 1.06 in the HLW-NG-Fe2-II sample compared with CS = 0.27 and QS = 1.07 in the 24 h melt sample. This suggests that the partitioning observed in the Lorentzian doublets is almost certainly statistical. There is a difference in the total paramagnetic Fe observed using both fitting methods, 71.6% in the Lorentzian and 71.5% in the xVBF, compared to 83.6% in the 1 h melt sample and this is coupled with an increase in the relative abundance of the magnetic, spinel phase, for which two sextets are now resolved with magnetic field strength, H, values corresponding to Magnetite (Fe_3O_4) [93]. There is no suggestion that the structure of Fe in the HLW-NG-Fe2-II glass approaches the structure in the HLW-NG-Fe2 glass with 24 h melting time, as the Raman would suggest, the main structural change with melting time is the increase in the relative abundance of magnetic phase.

3.6. X-ray fluorescence spectroscopy

Final glass compositions, as determined by ICP-MS, for Li_2O and B_2O_3, and XRF for most of the remaining elements, are compared to the target composition in Table 9. Nominal values CeO_2 and La_2O_3 as these were not detectable by the instrument not available in the XRF OXI program used [69]. The SO_3 has not been retained in either of the glasses within the limits of detection of XRF; its evolution may arise during either sample melting, or XRF sample preparation [68], or both. There is loss of Na, −3.23 wt% and −2.26 wt% of the HLW-NG-Fe2 and HLW-NG-Fe2-II glass samples, respectively. This loss is unlikely to be due to volatilisation during the

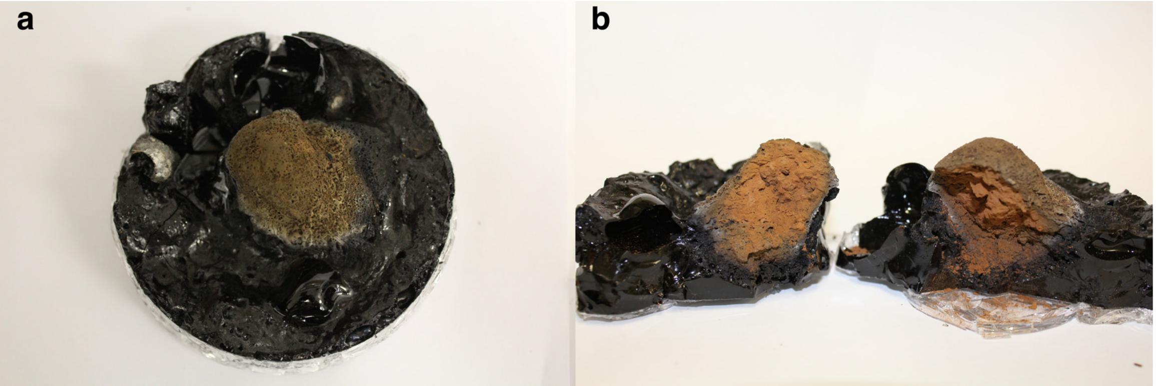

Fig. 15. Images of the laboratory scale melter cold cap sample of the HLW-NG-Fe2-II feed.

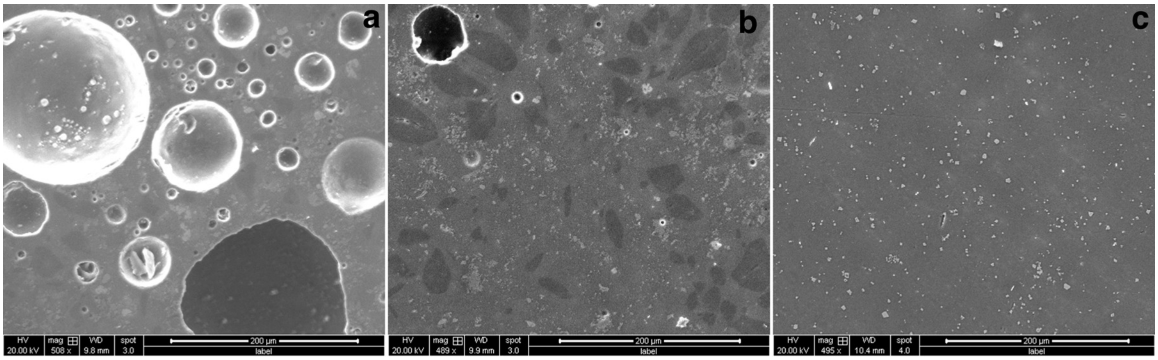

Fig. 16. SEM images of three regions of the LSM sample from the top feed region (left), the middle feed-to-glass region (middle), and the glass region (right).

initial melting, since there is no loss of B and little loss of Li, by ICP-MS, however it may be volatilised in the fused bead preparation process [68], or an issue with quantification by XRF since Na is the lower limit of detection of the instrument. Fe_2O_3 is shown to have increased in both samples. From Rietveld refinement of the X-ray powder diffraction patterns of the glass samples there is 1.68 and 1.79 wt% Fe_3O_4 crystallinity in the HLW-NG-Fe2 and HLW-NG-Fe2-II which, if misrepresented as Fe_2O_3 in the OXI program used to analyse XRF [69], would increase the wt% Fe_2O_3 output by 0.06 wt%, however this does not account for the 1.8 and 1.7 wt% increases in Fe_2O_3 content reported. For the purpose of this study, we are satisfied that there is consistency in the Fe_2O_3 content between the two samples.

3.7. Laboratory scale melter sample analysis

Feeding tests were performed on each of the feeds to determine their suitability for testing in the Laboratory Scale Melter. The HLW-NG-Fe2 feed was highly viscous, and the test had to be stopped multiple times to unblock the feed tubes. The HLW-NG-Fe2-II feed experienced no feeding issues during this test and was therefore a suitable feed to run in the Laboratory Scale Melter. The Laboratory Scale Melter (LSM) testing was performed with the reduced iron feed, HLW-NG-Fe2-II, to evaluate the results of the Stages of Melting study in a more representative system. During the test there were no feeding issues, and a sufficient sample, based on visual observation of the cold cap thickness, was produced with 40 min of feeding at a rate of 7–10 ml min^{-1}, the conversion rate was similar to previous LSM tests with this system [65,109]. The crucible was removed from the furnace and quenched on a copper block after feeding was stopped. The final LSM sample shown in Fig. 15 was broken from the rest of the crucible and split into two parts for further analysis.

SEM images of the LSM sample are shown in Fig. 16, followed by EDX of the SE images in, Fig. 17, from the top feed portion of the sample down to the glass region. In the top feed and foaming region where bubbles are clearly shown and undissolved phases are present, the EDX shows the presence of large Si-rich crystals, Zr-rich crystals and Fe-rich crystals. This is consistent with the XRD collected for the Stages of Melting samples between 600 and 700 °C (Fig. 5). In the mid feed-to-glass region small bubbles remain and there are undissolved Si-rich (quartz) and Fe-rich (haematite) crystals. The glassy region contains spinel crystals: as in the glass samples from the Stages of Melting study, the crystals are much larger in this sample with a volume of 7.11 μm^3. The increase in size may be due to the larger sample size or a different temperature profile [110], as observed in a previous comparison of an LSM samples heat-treated feed samples [66].

4. Discussion

4.1. Foaming behaviour and gas evolution

By using $FeC_2O_4{\cdot}2H_2O$ as a raw material in the HLW-NG-Fe2 feed, rather than $Fe(OH)_3$, we have observed a reduction in peak foaming of 50.0 ± 10.8% equating to a reduction of 11.1 ± 2.4% maximum porosity, from the values in Table 3. This foam reduction is greater than observed previously in the HLW-Al-19 feed with the same change of raw material [44]. The difference in the volume of foam, in Fig. 2, is due to the temperature at which the gases evolve. The large evolution of H_2O, CO and CO_2 in HLW-NG-Fe2-II, from the raw material, occurs prior to the foaming onset. Once the porosity is closed, ~700 °C, very little gas evolves from this feed. Foaming in the HLW-NG-Fe2-II feed starts at a higher temperature, suggesting either the retardation of the dissolution of the raw materials into a glass forming melt, or a lower viscosity of the

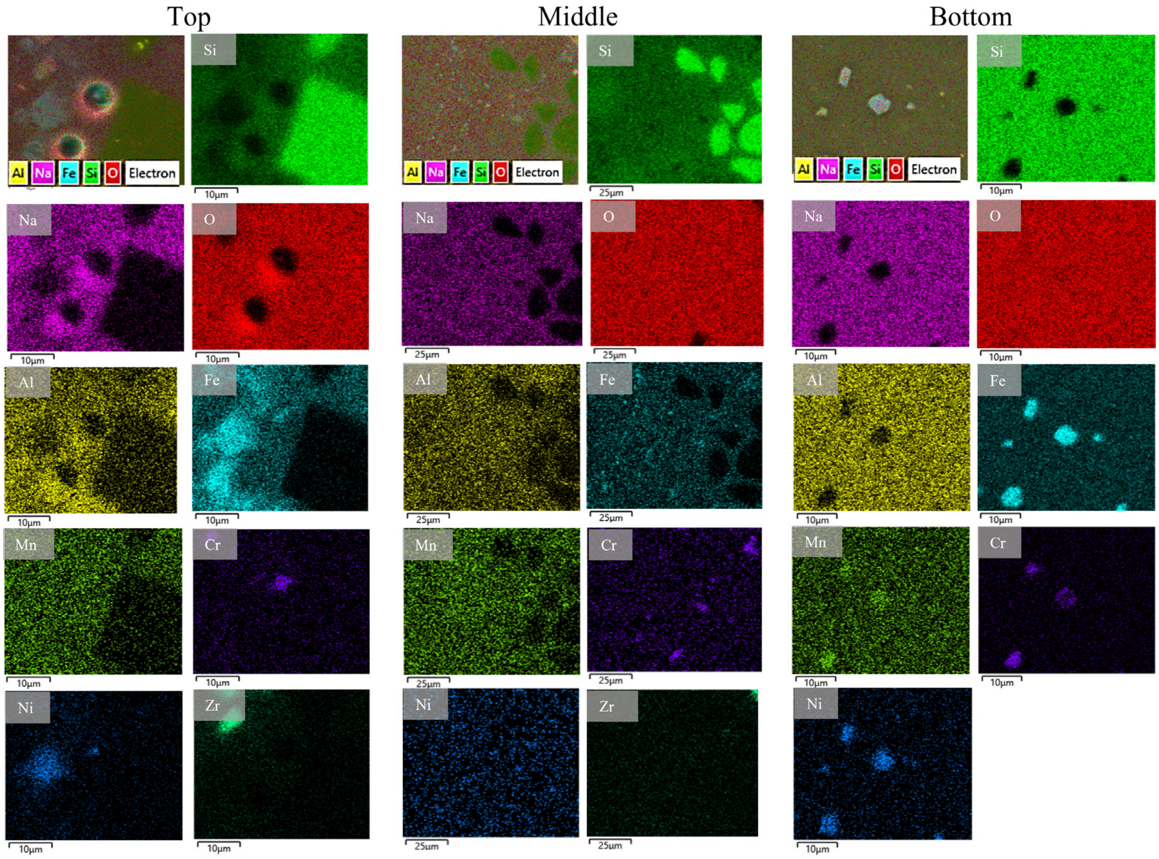

Fig. 17. Elemental maps by energy dispersive X-ray spectroscopy of the of the LSM sample from the top feed region (left), the middle feed-to-glass region (middle), and the glass region (right).

Table 3
Foaming behaviour in the HLW-NG-Fe2 and HLW-NG-Fe2-II feeds during melting from FETs and TGA.

	HLW-NG-Fe2	HLW-NG-Fe2-II
Normalised Maximum Foam Volume	10.0 ± 2.1	5.0 ± 0.2
Maximum Porosity	0.90 ± 0.19	0.80 ± 0.03
Total gas evolved (% mass)	12.6 ± 0.51	20.5 ± 0.38
Temperature foam onset (°C)	600 ± 10	700 ± 10
Temperature foam collapse* (°C)	774 ± 10	775 ± 10

* Measured at peak foam height.

Table 4
Total evolved gases during melting of the HLW-NG-Fe2 and HLW-NG-Fe2-II feeds by integration of the EGA curves.

	Total evolved gas (mg kg^{-1} glass)	
Gases	HLW-NG-Fe2	HLW-NG-Fe2-II
CO_2	40,240	181,000
CO	10.8	35,200
O_2	5120	0.0
SO_2	149	0.0
NO	1030	316

glass-forming melt at the temperature of foam onset in the HLW-NG-Fe2 feed, allowing for gases to escape through open porosity. In the HLW-NG-Fe2 feed the earlier connection of a viscous melt means that a larger quantity of gases are trapped, forming bubbles and causing the much larger expansion. By TG-MS and EGA, in Figs. 3 and 4, the gases evolving above ~700 °C in the HLW-NG-Fe2 feed are CO_2, O_2 and SO_2.

While there is no apparent change in the redox state of the paramagnetic Fe with melting in the HLW-NG-Fe2 feed, there will be O_2 evolved during the formation of Fe_3O_4 and the redox states of other multivalent species in this feed have not been assessed, which could account for generation of some O_2. O_2 evolution is entirely suppressed in the HLW-NG-Fe2-II feed above 800 °C due to consumption of O_2 in reactions with CO and FeO.

4.2. Thermal decomposition of iron raw materials

Based on the thermal analysis results, we here propose potential decomposition pathways for the iron-bearing raw materials in each of the feeds. It is likely that both raw materials dehydrate by ~350 °C, based on evidence from both literature [111,112] and the TG-MS data collected for H_2O evolution, shown in Fig. 3.

$$FeC_2O_4{\cdot}2H_2O \rightarrow FeC_2O_4 + 2H_2O \tag{1}$$

$$Fe(OH)_3 \rightarrow \frac{1}{2}Fe_2O_3 + \frac{3}{2}H_2O \tag{2}$$

For the HLW-NG-Fe2 material, Rietveld analysis of the XRD patterns in Fig. 6 shows that by 600 °C both Fe_2O_3 and iron containing spinel structures have formed, as observed previously with this feed [44], and they increase in relative abundance at temperatures up to 800 °C. At temperatures above 800 °C the Fe-containing crystals dissolve into the melt, leaving traces of spinel crystals at 1150 °C.

The FeC_2O_4 raw material in the HLW-NG-Fe2-II feed has multiple potential pathways for decomposition: two reactions, described in Eqs. (3a)–(3c) and (4) [97], could conceivably occur. The increased evolution of CO and CO_2 shown by TG-MS and EGA in

Table 5
Fitted Rietveld parameters for spinel-type phases ($Fd\bar{3}m$ cubic) identified at each stage of melting in the HLW-NG-Fe2 feed.

Sample	Compound	ICDD Ref.	Lattice Constants (Å)	% of total crystallinity
600 °C	Trevorite ($NiFe_2O_4$)	00-044-1485	$a = 8.342(5)$	7.2(1)
700 °C	Trevorite (Fe_2NiO_4)	04-005-6873	$a = 8.326(3)$	8.67(1)
800 °C	Manganese Chromium Iron Oxide ($CrMnFeO_4$)	04-013-0049	$a = 8.392(3)$	14.19(1)
900 °C	Iron Oxide (Fe_3O_4)	04-009-8437	$a = 8.403(4)$	20.4(1)
1000 °C	Manganese Chromium Iron Oxide ($CrMnFeO_4$)	04-013-0049	$a = 8.409(5)$	33.0(1)
1100 °C	Magnesium Iron Oxide (Fe_2MgO_4)	04-012-1079	$a = 8.405(5)$	46.5(3)
1150 °C	Magnetite (Fe_3O_4)	01-076-1849	$a = 8.401(04)$	100.0(4)

Table 6
Fitted Rietveld parameters for spinel-type phases ($Fd\bar{3}m$ cubic) identified at each stage of melting in the HLW-NG-Fe2-II feed.

Sample	Compound	ICDD Ref.	Lattice Constants (Å)	% of total crystallinity
600 °C	–	–	–	0.00
700 °C	Trevorite ($NiFe_2O_4$)	04-014-8286	$a = 8.368(2)$	30.0(2)
800 °C	Magnetite (Fe_3O_4)	04-008-4511	$a = 8.401(3)$	16.44(7)
900 °C	Magnetite (Fe_3O_4)	04-002-5632	$a = 8.399(3)$	37.6(1)
1000 °C	Magnetite (Fe_3O_4)	01-080-6404	$a = 8.404(3)$	57.7(4)
1100 °C	Ni^{2+} Bearing Magnetite ($Fe_{2.8}Ni_{0.2}O_4$)	04-020-9383	$a = 8.400(3)$	35.6(4)
1150 °C	Magnetite (Fe_3O_4)	01-088-0866	$a = 8.391(2)$	100.0(1)

Figs. 3 and 4, respectively, are consistent with either or both of these reactions. The suppression of O_2 evolution, measured by EGA, also supports the consumption of O_2 in the first reaction Eqs. (3a)–(3c). From XRD (Figs. 5 and 6), spinel crystals form at 700 °C and then haematite forms at 800 °C. This would suggest that the reaction in Eq. (4) occurs, and that some spinel oxidises to form haematite, Fe_2O_3, by 800 °C, which would also explain some of the consumption of O_2.

$$FeC_2O_4 \rightarrow FeO + CO + CO_2 \tag{3a}$$

$$CO + \frac{1}{2}O_2 \rightarrow CO_2 \tag{3b}$$

$$2FeO + \frac{1}{2}O_2 \rightarrow Fe_2O_3 \tag{3c}$$

$$3FeC_2O_4 \rightarrow Fe_3O_4 + 4CO + 2CO_2 \tag{4}$$

4.3. Structure and morphology during melting

^{57}Fe Mössbauer analysis supports the decomposition pathways of iron raw materials suggested above in Eqs. (3) and (4). The presence of paramagnetic Fe^{3+} and Fe^{2+} doublets in the HLW-NG-Fe2-II sample heated to 600 °C suggests that while some of the iron in the raw material has oxidised, it has not formed magnetic crystalline components at this temperature, instead forming unstable FeO; the later formation of these magnetic crystalline components again explains the consumption of some oxygen. Oxidation in the temperature range 400–800 °C has been observed in crucible studies of glass batches and waste feeds containing initially reduced Fe [113] and with added sucrose additions [29]. The transition from haematite crystals to spinel crystals is expected to occur as temperature increases [44] and is reflected in the Rietveld analysis of the XRD patterns in Fig. 6.

Tables 5 and 6. In the final glass samples the spinel phase formed has been identified by XRD, Tables 5 and 6, as having a structure with very similar lattice parameters to Fe_3O_4 but containing Cr, Ni and Mn inclusions, as confirmed by SEM/EDX (Figs. 7 and 9) The fitted parameters from the Mössbauer spectra for the glass samples are consistent with these inclusions, as they have similar magnetic field strengths to magnetite but with slightly different CS and QS to those which would be expected from pure magnetite [93].

The relative abundances of amorphous phase and quartz dissolution can both be indicators of melting rates. Based on the XRD (Fig. 6) and SEM/EDX (Figs. 7 and 9) results, there is no measured difference in amorphous phase fraction and melting rate between the two feeds above the foaming temperature [5]. The dissolution rate of quartz phase and the emergence of the amorphous phase as a function of temperature are similar for both feeds, indicating similar melting rates. The main structural changes occurring upon heating, i.e., from crystalline raw materials to melt, occurs between 600 and 900 °C - where most of the foaming occurs – for both feed materials.

4.4. Characterisation of the final glass product

X-ray fluorescence spectroscopy with ICP-MS for B and Li compositional analysis (Table 9) and SEM/EDX (Figs. 7 and 9) of the final glass products for both HLW-NG-Fe2 and HLW-NG-Fe2-II show that the compositions of the final glasses are similar. The levels of crystallinity in the final glasses are also similar, with the original feed having 1.68 wt% and 0.05 vol%, by XRD and SEM respectively, and the modified feed having 1.79 wt% and 0.07 vol%. Within uncertainties associated with these measurements, they can reasonably be considered to be equal. These samples were quenched in air and the levels of crystallinity could change when the glasses are poured in the JHCM system and cooled by canister centreline cooling [114,115]. Given the similarity in the final glasses studied here, there is no indication that any desirable properties for long-term durability have been altered as a result of the change in raw material, although long-term durability tests would be required to confirm this. The present study suggests that the 4.6 wt% carbon addition to the feed via the $FeC_2O_4{\cdot}2H_2O$ raw material does not produce a glass with an appreciable Fe^{2+} content and, therefore, there is very little chance of metallic precipitation. Previous tests of $FeC_2O_4{\cdot}2H_2O$ as a raw material show very little Fe^{2+} content in the final glass; in LAW feed studies 2.4–4.4% of the iron was Fe^{2+} in the final glass [27], in the HLW-Al-19 feed the glass was "slightly more reduced" than the glass batched with $Fe(OH)_3$ [44]. Since over-reduction and chemical durability are some of the main concerns, associated with redox manipulation of HLW feeds [14,19,56] this work also supports improved understanding of carbon additions or other methods of redox manipulation to waste feeds with high multivalent species contents [14].

Table 7
Hyperfine fitting parameters for ^{57}Fe Mössbauer spectra of the heat-treated feed samples at 800, 1000 and 1150 °C for the HLW-NG-Fe2 (NG-Fe2) and HLW-NG-Fe2-II (NG-Fe2-II). CS relative to α-Fe. CS ± 0.02 mm s^{-1}, QS ± 0.02 mm s^{-1}, H ± 0.5 T, Area ± 2%.

Feed	Temp (°C)	Component	CS (mm s^{-1})	QS (mm s^{-1})	H (T)	Area (%)
NG-Fe2	600	Doublet 1	0.33	1.12		9.1
		Sextet 1	0.37		51.6	53.0
		Sextet 2	0.36		49.7	26.0
		Sextet 3	0.35		46.4	11.9
NG-Fe2-II	600	Doublet 1	0.38	0.66		39.0
		Doublet 2	0.38	1.09		54.0
		Doublet 3	0.89	2.59		7.0
NG-Fe2	800	Doublet 1	0.25	0.95		25.0
		Sextet 1	0.36		50.9	62.6
		Sextet 2	0.41		44.3	12.4
NG-Fe2-II	800	Doublet 1	0.25	1.03		33.4
		Sextet 1	0.37		50.8	43.0
		Sextet 2	0.32		45.4	23.6
NG-Fe2	1000	Doublet 1	0.27	1.25		34.3
		Doublet 2	0.27	0.79		23.0
		Sextet 1	0.38		51.1	26.5
		Sextet 2	0.33		47.6	16.1
NG-Fe2-II	1000	Doublet 1	0.28	1.29		37.3
		Doublet 2	0.28	0.80		30.0
		Sextet 1	0.39		51.0	8.5
		Sextet 2	0.33		47.6	24.2
NG-Fe2	1150	Doublet 1	0.26	0.78		39.0
		Doublet 2	0.27	1.33		41.0
		Sextet 1	0.25		48.2	20.0
NG-Fe2-II	1150	Doublet 1	0.25	0.79		35.0
		Doublet 2	0.27	1.30		48.0
		Sextet 1	0.43		47.5	16.0

Table 8
Hyperfine fitting parameters for ^{57}Fe Mössbauer spectra of the HLW-NG-Fe2-II glass sample heated to 1150 °C for 24 h. CS relative to α-Fe. CS ± 0.02 mm s^{-1}, QS ± 0.02 mm s^{-1}, H ± 0.5 T, Area ± 2%.

Feed	Temp (°C)	Component	CS (mm s^{-1})	QS (mm s^{-1})	H (T)	Area (%)
NG-Fe2-II	1150	Doublet 1	0.27	0.82		32.6
24 h		Doublet 2	0.27	1.31		39.0
melt		Sextet 1	0.35		47.8	19.4
		Sextet 2	0.38		43.4	9.0

The small but non-negligible structural differences in these samples observed from Raman spectroscopy (Figs. 10 and 11) require further investigation to understand, the theory of an increase in Fe^{3+} content in the glass leading to a decrease in danburite ring units [85–87] cannot be adopted without further study since ^{57}Fe Mössbauer spectroscopic analysis showed no change in Fe^{3+} content between the glass samples (see Table 7). Raman spectroscopy of the HLW-NG-Fe2-II glass sample melted for 24 h infers that this structural difference is transient and the structure approaches that of the HLW-NG-Fe2 glass with melting time, but ^{57}Fe Mössbauer spectroscopy did not identify any structural change in Fe. Further investigation is required to identify this structural irregularity and determine whether it will have any effect on the long-term chemical durability of the glassy phase.

4.5. Application in a laboratory scale melter

The Laboratory Scale Melter test with the HLW-NG-Fe2-II feed produced a sufficient sample with no feeding or excessive foaming issues. The presented SEM/EDX results in Fig. 16, of the glassy region of the representative cold cap sample, reflect those of the glass prepared by benchtop scale melting. The EDX maps, (Fig. 17) of the sample at lower temperatures are also consistent with XRD analysis (Figs. 5 and 6) of samples at 600, 700 and 800 °C. Both small bubbles and larger cavities are observed in the quenched LSM sample, consistent with the expectations of a realistic cold cap [4,40]. The successful increase in scale from the induction-melted Stages of Melting samples (Sections 2.2–2.5) to the more representative LSM system (Section 2.7) is promising for the potential processability of a feed with initially reduced iron, and a lower viscosity than the original feed in full-scale melters; validation of the use of laboratory-scale melters to predict full-scale melter behaviour is currently being modelled computationally, and the properties of feeds experiencing different redox conditions will ais this modelling [40,61,116]. While the form of iron entering the melter is not something that is practical to alter, the implications of the reduced viscosity, addition of carbon and structural behaviour during melting studied with the $FeC_2O_4{\cdot}2H_2O$ raw material will help guide future research on the mechanisms of foaming and methods for reduction of foam.

5. Conclusions

A decrease of 50.0 ± 10.8% in the maximum normalised volume of the HLW-NG-Fe2 feed during melting is observed when it is prepared using $FeC_2O_4{\cdot}2H_2O$ rather than $Fe(OH)_3$ as the iron source. The reduction in foaming is consistent with previous studies of carbonaceous material additions and alternative raw materials during vitrification. The mechanisms of foam reduction in the reduced iron feed have been explored through the decomposition pathways of the raw materials, by both EGA and TG-MS. A rigorous study of the structural changes during melting by XRD, SEM/EDX, ^{57}Fe Mössbauer and Raman spectroscopies has been undertaken, showing that the feeds deviate in properties most notably between

Table 9
Analysed compositions of HLW-NG-Fe2 and HLW-NG-Fe2-II glasses by X-ray fluorescence (XRF) spectroscopy compared with the nominal composition.

Oxide	Nominal Composition (wt%)	HLW-NG-Fe2 (wt%)	HLW-NG-Fe2-II (wt%)
SiO_2	41.02	41.2(2)	41.13(2)
Na_2O	13.36	10.1(2)	11.1(2)
B_2O_3	13.79	15.49*	14.46*
Li_2O	1.56	1.18*	1.38*
MgO	0.16	0.36(2)	0.00
Fe_2O_3	16.12	17.94(3)	17.86(3)
Al_2O_3	5.59	6.6(1)	6.03(1)
CaO	0.52	0.61(1)	0.60(1)
ZrO_2	1.13	0.94(03)	1.18(03)
SrO	0.20	0.16(01)	0.16(01)
SO_3	0.22	0.00	0.00
P_2O_5	0.78	0.60(3)	0.65(3)
MnO	3.95	3.20(1)	3.63(1)
PbO	0.63	0.66(05)	0.73(5)
NiO	0.47	0.45(04)	0.54(4)
Cr_2O_3	0.25	0.25(1)	0.29(1)
CeO_2	0.12	0.12**	0.12**
ZnO	0.03	0.03(01)	0.03(01)
La_2O_3	0.09	0.09**	0.09**
Sum	100.00	100.00	100.00

* Measured by ICP.
** Nominal Values.

600 and 800 °C of the temperatures investigated, and equilibrate up to glass melting temperatures. At the upper melt temperature, they are structurally similar but not identical: the differences in structure converge when the glass is melted for 24 h, suggesting transient structures that warrant further investigation. Key melting rate indicators of the two feeds, such as dissolution of silica and temperature of foam collapse, are similar for the two feeds, meaning a similarly high melting rate would be achieved with this change of raw material. Neither of the final glasses studied here contain appreciable quantities of Fe^{2+}, within the detection limits of ^{57}Fe Mössbauer spectroscopy and approximately equal quantities of spinel phase were present in the two final glasses.

While manipulation of iron redox in the feed before entering the melter may not be a practical option for the Hanford site, the results are consistent with the view that addition of a reductant, such as a carbon source, or other methods of redox manipulation before or during melting, can be a key enabler for foam reduction in this high-iron feed. Furthermore, the structures of the final glasses remain similar, and there is low risk of precipitation of metallic species or alteration of the desirable properties of the final glass. This has implications when evaluating methods of redox control for the operation and efficiency of processing high-iron radioactive waste feeds in JHCMs relevant to the US Hanford site melters and others.

Declaration of Competing Interest

The authors declare that they have no known competing financial interests or personal relationships that could have appeared to influence the work reported in this paper.

CRediT authorship contribution statement

Jessica C. Rigby: Conceptualization, Investigation, Writing – original draft, Visualization, Project administration. **Derek R. Dixon:** Conceptualization, Methodology, Investigation, Writing – review & editing. **Derek A. Cutforth:** Investigation, Methodology. **Jose Marcial:** Conceptualization, Methodology, Writing – review & editing. **Jaroslav Kloužek:** Formal analysis, Investigation. **Richard Pokorný:** Conceptualization, Methodology, Writing – review & editing. **Albert A. Kruger:** Supervision, Funding acquisition, Writing – review & editing. **Alex Scrimshire:** Formal analysis, Investigation. **Anthony M.T. Bell:** Supervision, Writing – review & editing. **Paul A. Bingham:** Supervision, Writing – review & editing, Funding acquisition.

Acknowledgments

The authors would like to thank Jaime George, Seung Min Lee and Pavel Hrma for their technical advice and insightful discussions. The authors acknowledge, with thanks, funding from the US Department of Energy Office of River Protection and from Sheffield Hallam University.

Supplementary materials

Supplementary material associated with this article can be found, in the online version, at doi:10.1016/j.jnucmat.2022.153946.

References

[1] A. Goel, J.S. McCloy, R. Pokorny, A.A Kruger, Challenges with vitrification of Hanford high-level waste (HLW) to borosilicate glass – an overview, J. Non Cryst. Solids X 4 (2019) 100033.
[2] R.E. Gephart, A short history of waste management at the Hanford site, Phys. Chem. Earth 35 (2010) 298–306.
[3] US Department of Energy. Hanford tank waste retrieval, treatment, and disposition framework. (2013). Available at: https://www.energy.gov/em/nnmcab/downloads/hanford-tank-waste-retrieval-treatment-and-disposition-framework (Accessed: 26 July 2022)
[4] R. Pokorný, P Hrma, Model for the conversion of nuclear waste melter feed to glass, J. Nucl. Mater. 445 (2014) 190–199.
[5] R. Pokorný, Z.J. Hilliard, D.R. Dixon, M.J. Schweiger, D. Post Guillen, A.A. Kruger, P. Hrma, One-dimensional cold cap model for melters with bubblers, J. Am. Ceram. Soc. 98 (2015) 3112–3118.
[6] D.F. Bickford, R.B. Diemer, Redox control of electric melters with complex feed compositions I. Analytical methods and models, J. Non. Cryst. Solids 84 (1986) 276–284.
[7] P. Hrma, R. Pokorný, The Office of River Protection Cold Cap and Melt Dynamics Technology Development and Research Plan, Pacific Northwest National Laboratory, Richland, WA (United States), 2016 PNNL-25350.
[8] J.H. Jarrett, J.E. Minor, LFCM vitrification technology quarterly progress report PNL-5470-4, Pacific Northwest National Laboratory, Richland, WA United States, 1986.
[9] P. Hrma, A.A. Kruger, Nuclear waste glasses: continuous melting and bulk vitrification, Adv. Mater. Res. 39–40 (2008) 633–640.
[10] D.A. Pierce, P. Hrma, J. Marcial, B.J. Riley, M.J Schweiger, Effect of alumina source on HLW-feed melting process, Int. J. Appl. Glass Sci. 3 (2012) 59–68.

[11] H.T. Blair, J.M. Lukacs, Investigation of Foaming During Nuclear Defense Waste Solidification by Electric Melting, Pacific Northwest National Laboratory, Richland, WA (United States), 1980 PNL-3552.

[12] C.M. Jantzen, M.E. Stone, Role of Manganese Reduction/Oxidation (REDOX) on Foaming and Melt Rate in High Level Waste (HLW) Melters (U), Savannah River National Laboratory, Aiken, SC (United States), 2007 WSRC-STI-2006-00066.

[13] M.A. Cable, A century of developments in glassmelting research, J. Am. Ceram. Soc. 81 (2005) 1083–1094.

[14] Kruger, A.A. Matlack, K.S. Pegg, I.L. Kot, W.K. & Joseph, I. Redox control for Hanford HLW feeds. VSL-12R2530-12. Vitreous State Laboratory, Catholic University of America, D.C., United States: (2012).

[15] F.W. Adams, Fining of Glass, United States Patent Office US2274643A (1942) https://patents.google.com/patent/US2274643.

[16] Knavish, L.A. & Harrell, W.C. Melting glass with oxidation control and lowered emissions. United States Patent Office. US5006144 (1991). Available at: https://patentimages.storage.googleapis.com/73/43/f5/20cb5a83804e4a/US5006144.pdf (Accessed: 26 July 2022).

[17] D.F. Bickford, Redox control of electric melters with complex feed compositions II. Preliminary limits for radioactive waste melters, J. Non. Cryst. Solids 84 (1986) 285–291.

[18] V. Jain, Survey of Solidification Process Technologies, Nuclear Regulatory Commission, San Antonio, TX (United States), 1998.

[19] R.G. Seymour, Development of the High-Level Waste High-Temperature Melter Feed Preparation Flowsheet for Vitrification Process Testing, Oak Ridge. TN, United States, 1995 WHC-SD-WM-SP-008.

[20] D.F. Bickford, A.S Choi, Control of High Level Radioactive Waste-Glass Melters - Part 5: Modelling of Complex Redox Effects, WSRC, Aiken, SC. (United States), 1991 MS–91-101.

[21] K.S. Matlack, I. Joseph, W. Gong, I.S. Muller, I.L. Pegg, Glass formulation development and DM10 melter testing with ORP LAW glasses VSL-09R1510-2, Vitreous State Laboratory, Washington D. C., United States, 2009.

[22] K.D. Weimers, The Effect of HWVP Feed Nitrate and Carbonate Content on Glass Redox Adjustment, PNNL, Richland, WA. (United States), 1998 11044.

[23] K.D. Weimers, M.H. Langowski, M.R. Powell, D.E. Larson, Evaluation of HWVP Feed Preparation Chemistry for an NCAW Simulant-Fiscal Year 1991: Evaluation of Offgas Generation, Reductant Requirements and Thermal Stability, PNNL, Richland, WA (United States), 1996 Technical Report11029.

[24] T. Jin, D. Mar, D. Kim, B.L. Weese, A.A. Kruger, Reactions during conversion of simplified low-activity waste glass feeds, Thermochim. Acta 694 (2020) 178783.

[25] C.J. Appel, J. Kloužek, N. Jani, S. Lee, D.R. Dixon, P. Hrma, R. Pokorný, A.A. Kruger, M.J. Schweiger, Effect of sucrose on foaming and melting behavior of a low-activity waste melter feed, J. Am. Ceram. Soc. 102 (2019) 7594–7605.

[26] T. Jin, J. Chun, D.R. Dixon, D.S. Kim, J.V. Crum, C.C. Bonham, B.J. VanderVeer, C.P. Rodriguez, B.L. Weese, M.J. Schweiger, A.A. Kruger, P. Hrma, Melter feed viscosity during conversion to glass: comparison between low-activity waste and high-level waste feeds, J. Am. Ceram. Soc. 101 (2018) 1880–1891.

[27] Matlack, K.S. Muller, I.S. Callow, R.A. D'Angelo, N. Bardakci, T. Joseph, I. Pegg, I.L. Improving technetium retention in Hanford LAW glass – phase 2. VSL11R2260-1. Vitreous State Laboratory, Washington, D. C. United States (2011).

[28] A.A. Kruger, K.S. Matlack, W. Gong, I.L. Pegg, Small-scale melter testing with LAW simulants to assess the impact of higher temperature melter operations ORP-51809. VSL-04R4980-1, Vitreous State Laboratory, Washington, D. C., United States, 2012.

[29] D.S. Kim, C.Z. Soderquist, J.P. Icenhower, B.P. Mcgrail, R.D. Scheele, B.K. McNamara, L.M. Bagaasen, M.J. Schweiger, J.V. Crum, D.J. Yeager, J. Matyáš, L.P. Darnell, H.T. Schaef, A.T. Owen, A.E. Kozelisky, L.A. Snow, M.J. Steele, Tc Reductant Chemistry and Crucible Melting Studies with Simulated Hanford Low-Activity Waste, PNNL, Richland, WA (United States), 2005 -15131.

[30] I.S. Muller, C. Viragh, H. Gan, K.S. Matlack, I.L Pegg, Iron Mössbauer redox and relation to technetium retention during vitrification, Hyperfine Interact. 191 (2009) 17–24.

[31] C.Z. Soderquist, M.J. Schweiger, D.S. Kim, W.W. Lukens, J.S McCloy, Redox-dependent solubility of technetium in low activity waste glass, J. Nucl. Mater. 449 (2014) 173–180.

[32] D.F. Bickford, P. Hrma, B.W. Bowan, Control of radioactive waste glass melters: ii, residence time and melt rate limitations, J. Am. Ceram. Soc. 73 (1990) 2903–2915.

[33] Carl, D.E. West Valley Demonstration Project vitrification process equipment functional and checkout testing of systems (FACTS). DOE/NE/44139-64. West Valley Nuclear Services Co., Inc., West Valley, NY, United States (1990).

[34] J.M. Perez, et al., Vitrification process testing for reference HWVP waste PNL-SA-16887, Pacific Northwest National Laboratory, Richland, WA, United States, 1989.

[35] J.E. Josephs, M.E. Stone, Melt rate improvement for DWPF MB3: sugar addition Test (U) WSRC-TR-2001-00158, Westinghouse Savannah River Company, Aiken, SC, United States, 2001.

[36] D.E. Larson, Hanford high-level waste vitrification program at the Pacific Northwest National Laboratory: technology development - annotated bibliography. PNNL-10955, Pacific Northwest National Laboratory, Richland, WA, United States, 1996.

[37] C.M. Jantzen, Development of glass matrices for high level radioactive wastes, in: Handbook of Advanced Radioactive Waste Conditioning Technologies, Woodhead Publishing Limited, 2011, pp. 230–292, doi:10.1533/9780857090959.2.230.

[38] D.K. Peeler, T.B. Edwards, Impact of redox on glass durability: the glass selection process. WSRC-TR-2004-00135, Savannah River Technology Center, Aiken, SC., United States, 2004.

[39] R.G.C. Beerkens, J Van Der Schaaf, Gas release and foam formation during melting and fining of glass, J. Am. Ceram. Soc. 89 (2006) 24–35.

[40] D.P. Guillen, A.W. Abboud, R. Pokorný, Computational Experiments to Characterize Bubble Formation and Movement in Waste Glass Foam layer, Idaho National Lab (INL), Idaho Falls, ID (United States), 2019 INL/CON-18-52050-Rev 0.

[41] R. Pokorný, D.A. Pierce, P. Hrma, Melting of glass batch: model for multiple overlapping gas-evolving reactions, Thermochim. Acta 541 (2012) 8–14.

[42] D.S. Goldman, Melt foaming, foam stability and redox in nuclear waste vitrification, J. Non. Cryst. Solids 84 (1986) 292–298.

[43] R. Pokorný, A.A. Kruger, P. Hrma, Mathematical modeling of cold cap: effect of bubbling on melting rate, Ceram. Silik. 58 (2014) 296–302.

[44] D.P. Guillen, S. Lee, P. Hrma, J. Traverso, R. Pokorný, J. Kloužek, A.A. Kruger, Evolution of chromium, manganese and iron oxidation state during conversion of nuclear waste melter feed to molten glass, J. Non. Cryst. Solids 531 (2020) 119860.

[45] S. Lee, P. Hrma, R. Pokorný, J. Kloužek, W.C. Eaton, A.A. Kruger, Glass production rate in electric furnaces for radioactive waste vitrification, J. Am. Ceram. Soc. 102 (2019) 5828–5842.

[46] S. Lee, P. Hrma, R. Pokorný, J. Traverso, J. Kloužek, M.J. Schweiger, A.A. Kruger, Heat transfer from glass melt to cold cap: effect of heating rate, Int. J. Appl. Glass Sci. (2019) 1–13.

[47] K.S. Matlack, H. Gan, M. Chaudhuri, W.K. Kot, I.L. Pegg, I. Joseph, A.A. Kruger, Melter Throughput Enhancements for High-Iron HLW ORP-54002, Department of Energy, Office of River Protection, Richland, WA (United States), 2012.

[48] K.S. Matlack, I.L. Pegg, I. Joseph, W.K. Kot, Support for HLW Direct Feed - Phase 2 VSL-15R3440-1, Department of Energy, Office of River Protection, Richland, WA (United States), 2015.

[49] S.M. Lee, et al., Simplified melting rate correlation for radioactive waste vitrification in electric furnaces, J. Am. Ceram. Soc. 103 (2020) 5573–5578.

[50] P. Hrma, R. Pokorny, S.M. Lee, A.A. Kruger, Heat transfer from glass melt to cold cap: melting rate correlation equation, Int. J. Appl. Glass Sci. 10 (2) (2018) 1–8.

[51] P. Hrma, A.A. Kruger, Crystallization in Multicomponent Glasses, Department of Energy, Office of River Protection, Richland, WA (United States), 2009 ORP-42447.

[52] C.E. Lonergan, J. Rice, C. Skidmore, M.J. Schweiger, P Hrma, The effects of mixing multi-component HLW glasses on spinel crystal size, J. Nucl. Mater. 558 (2022) 153318.

[53] C.M. Jantzen, Development of glass matrices for high level radioactive wastes, in: Handbook of Advanced Radioactive Waste Conditioning Technologies, Woodhead Publishing Limited, 2011, pp. 230–292.

[54] P. Hrma, P. Schill, L. Nemec, Settling of Spinel in a High-Level Waste Glass Melter, Pacific Northwest National Lab., Richland, WA (United States), 2002 PNNL-13747.

[55] C. Brookes, M. Harrison, A. Riley, C Steele, The effect of increased waste loading on the durability of high level waste glass, Mater. Res. Soc. Symp. Proc. 1265 (2010) 109–114.

[56] G. Piepel, et al., Viscosity, and Electrical Conductivity Model Development. VSL-07R1230-1, Rev, Pacific Northwest National Laboratory, Richland, WA, United States, 2007.

[57] Gan, H. et al. Crystal settling, redox, and high temperature properties of ORP HLW and LAW glasses, VSL-09R1510-1. Vitreous State Laboratory, Catholic University of America, D.C., United States. (2009).

[58] K.S. Matlack, C. Viragh, W.K. Kot, I.L. Pegg, I. Joseph, Effect of the Form of Iron on HLW Melt Rate, Department of Energy, Office of River Protection, Richland, WA (United States), 2015 VSL-15R3430-1.

[59] Marcial, J. Kloužek, J., Vernerová, M., Ferkl, P. Lee, S. Cutforth, D. Hrma, P. Kruger, A.A. Pokorný, R. Effect of Al and Fe sources on conversion of high-level nuclear waste feed to glass. J. Nucl. Mater. 559, 153423 (2022).

[60] I.L. Pegg, Behavior of technetium in nuclear waste vitrification processes, J. Radioanal. Nucl. Chem. 305 (2015) 287–292.

[61] A.W. Abboud, D.P Guillen, Computational fluid dynamics modeling of bubbling in a viscous fluid for validation of waste glass melter modeling, Int. Top. Meet. Adv. Therm. Hydraul. 2016 (2016) 527–538 ATH 2016.

[62] D. Post Guillen, V. Agarwal, Incorporating Cold Cap Behavior in a Joule-heated Waste Glass Melter Model, Idaho National Laboratory, Idaho Falls, ID. (United States), 2013.

[63] M. Hujová, R. Pokorný, J. Kloužek, S. Lee, J.J. Traverso, M.J. Schweiger, a.A. Kruger, P. Hrma, Foaming during nuclear waste melter feeds conversion to glass: application of evolved gas analysis, Int. J. Appl. Glass Sci. 9 (2018) 487–498.

[64] D.R. Dixon, M.J. Schweiger, S. Lee, J.S. Heilman-Moore, P. Hrma, Effect of feed composition on cold-cap formation in laboratory-scale melter, in: Proceedings of the Annual Waste Management Symposium (WM2016), United States, Phoenix, AZ, 2016, pp. 1384–1391.

[65] B.J. Riley, J.V. Crum, W.C. Buchmiller, B.T. Rieck, M.J. Schweiger, J.D. Vienna, Initial Laboratory-Scale Melter Test Results for Combined Fission Product Waste, U.S. Department of Energy Waste Forms Campaign, Richland, WA (United States), 2009 PNNL-18781.

[66] D.R. Dixon, M.J. Schweiger, B.J. Riley, R. Pokorný, P Hrma, Temperature dis-

tribution within a cold cap during nuclear waste vitrification, Environ. Sci. Technol. 49 (2015) 8856–8863.

[67] A.M.T. Bell, D.J. Backhouse, W. Deng, J.D. Eales, E. Kilinc, K. Love, P. Rautiyal, J.C. Rigby, A.H. Stone, S. Vaishnav, G. Wei-Addo, P.A. Bingham, X-ray fluorescence analysis of feldspars and silicate glass: effects of melting time on fused bead consistency and volatilisation, Minerals 10 (5) (2020) 442.

[68] H.L. Giles, P.W. Hurley, H.W.M Webster, Simple approach to the analysis of oxides, silicates and carbonates using x-ray fluorescence spectrometry, X-Ray Spectrom. 4 (1995) 205–218.

[69] T. Degen, M. Sadki, E. Bron, U. König, G. Nénert, The high score suite, Powder Diffr. 29 (2014) S13–S18.

[70] S.D. Gates-Rector, T.N. Blanton, The powder diffraction file: a quality materials characterisation database, Powder Diffr 34 (2019) 352–360.

[71] H.M. Rietveld, A profile refinement method for nuclear and magnetic structures, J. Appl. Crystallogr. 2 (1969) 65–71.

[72] D.R. Neuville, B.O. Mysen, Role of aluminium in the silicate network: *in situ*, high-temperature study of glasses and melts on the join SiO_2-$NaAlO_2$, Geochim. Cosmochim. Acta 60 (1996) 1727–1737.

[73] D. Rancourt, Recoil Mössbauer Spectral Analysis Software, Intelligent Scientific Applications Inc, 1998.

[74] R. de Oro Calderon, C. Gierl-Mayer, H. Danninger, Application of thermal analysis techniques to study the oxidation/reduction phenomena during sintering of steels containing oxygen-sensitive alloying elements, J. Therm. Anal. Calorim. 127 (2017) 91–105.

[75] S. Lee, P. Hrma, J. Kloužek, R. Pokorný, M. Hujová, D.R. Dixon, M.J. Schweiger, A.A. Kruger, Balance of oxygen throughout the conversion of a high-level waste melter feed to glass, Ceram. Int. 43 (2017) 13113–13118.

[76] K.E. Sickafus, J.M. Wills, N.W Grimes, Structure of spinel, J. Am. Ceram. Soc. 82 (1999) 3279–3292.

[77] M.G. Brik, A. Suchocki, A. Kamińska, Lattice parameters and stability of the spinel compounds in relation to the ionic radii and electronegativities of constituting chemical elements, Inorg. Chem. 53 (2014) 5088–5099.

[78] M. Sezgin, B. Sankur, Survey over image thresholding techniques and quantitative performance evaluation, J. Electron. Imaging 13 (2004) 146–168.

[79] B.G. Parkinson, D. Holland, M.E. Smith, C. Larson, J. Doerr, M. Affatigato, S.A. Feller, A.P. Howes, C.R. Scales, Quantitative measurement of Q^3 species in silicate and borosilicate glasses using Raman spectroscopy, J. Non. Cryst. Solids 354 (2008) 1936–1942.

[80] A.K. Yadav, P Singh, A review of the structures of oxide glasses by Raman spectroscopy, RSC Adv. 5 (2015) 67583–67609.

[81] L. Chen, D.F. Zhang, P. Lv, J.D. Zhang, X. Du, W. Yuan, S. Nan, Z.H. Zhu, T.S. Wang, Evolutions of molecular oxygen formation and sodium migration in Xe ion irradiated borosilicate glasses, J. Non. Cryst. Solids 448 (2016) 6–10.

[82] L. Slavov, M.V. Abrashev, T. Merodiiska, C. Gelev, R.E. Vandenberghe, I. Markova-Deneva, I. Nedkov, Raman spectroscopy investigation of magnetite nanoparticles in ferrofluids, J. Magn. Magn. Mater. 322 (2010) 1904–1911.

[83] J.M. Li, A Huan, Interface effects on magnetoresistance and magnetic-field-reduced Raman scattering in magnetite, Phys. Rev. B Condens. Matter Mater. Phys. 61 (2000) 6876–6878.

[84] B. Cochain, D.R. Neuville, Determination of iron redox ratio in borosilicate glasses and melts from Raman spectra, Nucl. Fuel Cycle Sutain Future 19-23 May 2008 (2008) 1–7.

[85] B. Cochain, D.R. Neuville, G.S. Henderson, C.A. McCammon, O. Pinet, P. Richet, Effects of the iron content and redox state on the structure of sodiumborosilicate glasses: a Raman, Mössbauer and boron K-edge XANES spectroscopy study, J. Am. Ceram. Soc. 95 (2012) 962–971.

[86] D. Manara, A. Grandjean, D.R. Neuville, Advances in understanding the structure of borosilicate glasses: a raman spectroscopy study, Am. Mineral. 94 (2009) 777–784.

[87] Y.H. Yun, P.J. Bray, Nuclear magnetic resonance studies of the glasses in the system $K_2OB_2O_3P_2O_5$, J. Non. Cryst. Solids 30 (1978) 45–60.

[88] S. Barth, A. Feltz, Structure and ionic conduction in solids. VII. Ion conducting glasses in the system $Na_2ONb_2O_5P_2O_5$, Solid State Ion. 34 (1989) 41–45.

[89] J.L. Nelson, IHLW Waste Form Qualification Report for the Hanford Tank Waste Treatment and Immobilization Plant, US Department of Energy, Office of River Protection, Richland, WA (United States), 2010 24590-HLW-RP-T-RT-08-001 Rev. 0.

[90] D.F Bickford, A. Applewhite-Ramsey, C.M. Jantzen, K.G. Brown, Control of radioactive waste glass melters: I, preliminary general limits at Savannah river, J. Am. Ceram. Soc. 73 (10) (1990) 2896–2902.

[91] P.R. Hrma, P. Schill, L. Nemec, Settling of Spinel in a High-Level Waste Glass Melter, PNNL, Richland, WA (United States), 2001 13747.

[92] S.J. Oh, D.C. Cook, H.E Townsend, Characterisation of iron oxides commonly formed as corrosion products on steel, Hyperfine Interact. 112 (1998) 59–65.

[93] M. Darby Dyar, D.G. Agresti, M.W. Schaefer, C.A. Grant, E.C Sklute, Mössbauer spectroscopy of earth and planetary materials, Annu. Rev. Earth Planet. Sci. 34 (2006) 83–125.

[94] A. Deshkar, M. Ahmadzadeh, A. Scrimshire, E. Han, P.A. Bingham, D. Post Guillen, J. McCloy, A. Goel, Crystallization behavior of iron- and boron-containing nepheline ($Na_2O{\cdot}Al_2O_3{\cdot}2SiO_2$) based model high-level nuclear waste glasses, J. Am. Ceram. Soc. 4 (2018) 1–21.

[95] M. Darby Dyar, A review of Mössbauer data on inorganic glasses: the effects of composition on iron valency and coordination, Am. Mineral. 70 (1985) 304–316.

[96] D. Smrčka, V. Procházka, P. Novák, J. Kašlík, V. Vrba, Iron oxalate decomposition process by means of Mössbauer spectroscopy and nuclear forward scattering, AIP Conf. Proc. 1781 (2016) 020012.

[97] M.C. D'Antonio, A. Wladimirsky, D. Palacios, L. Coggiola, A.C. González-Baró, E.J. Baran, R.C. Mercader, Spectroscopic investigations of iron(II) and iron(III) oxalates, J. Braz. Chem. Soc. 20 (2009) 445–450.

[98] B. Fultz, E.N. Kaufmann, Mössbauer spectrometry, Characterisation of Materials, John Wiley, New York, (United States), 2012.

[99] J.J. Shrotri, C.E. Deshpande, S.K. Date, S.B. Ogale, Chemical passivation of unstable FeO - a Mössbauer study, Hyperfine Interact. 28 (1986) 733–736.

[100] T. Nishida, ^{57}Fe and ^{119}Sn-Mössbauer effect of oxide glasses, J. Radioanal. Nucl. Chem. 182 (1994) 451–476.

[101] C.A. Gorski, M.M. Scherer, Determination of nanoparticulate magnetite stoichiometry by Mössbauer spectroscopy, acidic dissolution, and powder X-ray diffraction: a critical review, Am. Mineral. 95 (2010) 1017–1026.

[102] M. Ahmadzadeh, A. Scrimshire, P.A. Bingham, A. Goel, Structural role of iron in nepheline-based aluminosilicates for nuclear waste applications, in: Proceedings of the WM2018 Conference, Phoenix, AZ (United States), 2018.

[103] S. Nakamura, A. Fuwa, Spin order in $FeCr_2O_4$ observed by mössbauer spectroscopy, Phys. Procedia 75 (2015) 747–754.

[104] A.K. Sijo, U.M. Basheer Al-Naib, Tailoring of the magnetic and structural properties of nanosized ferrites, Recent Advances in Porous Ceramics, 97, IntechOpen, 2018 (Ed.).

[105] A.K. Sijo, V.K. Jha, L.S. Kaykan, D.P. Dutta, Structure and cation distribution in superparamagnetic $NiCrFeO_4$ nanoparticles using Mössbauer study, J. Magn. Magn. Mater. 497 (2019) 166047.

[106] J.D. Arboleda, O. Arnache, M.H. Aguirre, R. Ramos, A. Anadón, M.R. Ibarra, Evidence of the spin Seebeck effect in Ni-Zn ferrites polycrystalline slabs, Solid State Commun. 270 (2018) 140–146.

[107] G.A. Sawatzky, F. Van Der Woude, A.H. Morrish, Mössbauer study of several ferrimagnetic spinels, Phys. Rev. 187 (1969) 747–757.

[108] D.S. Kim, M.J. Schweiger, W.C. Buchmiller, J. Matyáš, Laboratory Scale Melter for Determination of Melting Rate of Waste Glass Feeds, PNNL, Richland, WA (United States), 2012 21005.

[109] D.F. Bickford, C.M. Jantzen, Devitrification of defense nuclear waste glasses: role of melt insolubles, J. Non. Cryst. Solids 84 (1986) 299–307.

[110] S.K. Zaware, S.S. Jadhav, Kinetics and mechanism of thermal decomposition od binary mixture of ferrous oxalate and copper oxalate in the (1:2) mole ratio, Int. J. Eng. Res. 1 (2012) 1–5.

[111] M. Hermanek, R. Zboril, M. Mashlan, L. MacHala, O. Schneeweiss, Thermal behaviour of iron(II) oxalate dihydrate in the atmosphere of its conversion gases, J. Mater. Chem. 16 (2006) 1273–1280.

[112] V. Carles, P. Alphonse, P. Tailhades, A. Rousset, Study of thermal decomposition of $FeC_2O_4{\cdot}2H_2O$ under hydrogen, Thermochim. Acta 334 (1999) 107–113.

[113] S.L. Marra, C.M. Jantzen, Characterization of Projected DWPF Glasses Heat Treated to Simulate Canister Centerline Cooling, Westinghouse Savannah River Co., Aiken, SC (United States), 1993 WSRC-TR–92-142.

[114] B.J. Riley, J.A. Rosario, P.R. Hrma, Impact of HLW Glass Crystallinity on the PCT Response, Pacific Northwest National Lab., Richland, WA (United States), 2002 PNNL-13491.

[115] D.R. Dixon, M.J. Schweiger, B.J. Riley, R. Pokorný, P. Hrma, Cold-cap temperature profile comparison between the laboratory and mathematical model, in: Proceedings of the WM2015 Conference, Phoenix, AZ (United Sates), 2015, pp. 1–9.